Evaluation of the Urban Climate Model PALM-4U over Hilly Terrain Using Wind and Turbulence Observations

Olga Kiseleva[1,*], Leonhard Gantner[1], Norbert Kalthoff[1], Meinolf Kossmann[2], Christopher Holst[3]

[1] Institute of Meteorology and Climate Research Troposphere Research (IMKTRO)
[2] Climate and Environment Consultancy, Deutscher Wetterdienst (DWD), Offenbach am Main, Germany
[3] Institute of Meteorology and Climate Research Atmospheric Environmental Research (IMKIFU), Karlsruhe Institute of Technology, Karlsruhe, Germany

Abstract

We used boundary layer observations in the Stuttgart area from two summer episodes for model evaluation of the urban climate model PALM-4U. In summer 2017, radiosondes and Doppler lidars were operated, and the lidar virtual tower technique was applied to provide vertical profiles of wind speed and direction at different sites. In summer 2018, two Doppler lidars were operated in vertical stare mode providing vertical wind speeds and their variances. PALM-4U with grid spacings of 10 m in 2018 and 40 m in 2017 was driven by COSMO analysis data. The PALM-4U output data were evaluated with the observations at the corresponding sites.

For 14 to 15 August 2017, the normalised root mean square error (NRMSE) between simulated and measured wind speed time series at 100 m agl is about 0.5, except for the last hours of the investigated period. The RMSE for wind direction is 30–35°. At 700 m agl, the NRMSE for wind speed is 0.2–0.3 and the RMSE for wind direction is about 15°. The greater NRMSE differences found in the night and morning of 15 August can be explained by differences between the observed and simulated height of the low-level jet which caused stronger simulated turbulent downward mixing of momentum in the morning.

On 20 June 2018, the daytime convective boundary-layer evolution was well represented in the model. However, as the wind speed was low, 1-h integration times turned out to be not suitable for model evaluation because the uncertainty in variances of the vertical wind is considerable (50%). To overcome the poor statistics due to the low number of eddies dominating, 3-h integration times turned out to be necessary. For these time intervals, the simulated profiles lie within the error bars of the observations. Theoretical considerations provide suggestions for experimental set-ups and synoptic conditions to capture vertical profiles allowing model evaluations under convective conditions based on 1-h intervals.

Keywords: Urban climate under change (UC)2; Stuttgart area; atmospheric boundary layer; Doppler lidar; PALM-4U; LES; model evaluation

1 Introduction

The climate and air quality of cities are determined by meteorological and air-chemical processes, including surface-atmosphere exchange. Especially over complex terrain, several atmospheric processes superimpose on different scales and turbulent mixing, slope- and valley winds as well as capping inversions are decisive factors influencing the urban climate (e.g., Landsberg, 1981; Baumbach and Vogt, 2003; Oke et al., 2017). One of the relevant parameters describing vertical turbulent mixing in the atmospheric boundary layer (ABL) is the variance of vertical wind speed, σ_w^2. Therefore, observations of this parameter have been performed for several decades based on aircraft, wind profilers, and Doppler lidars (e.g., Wyngaard et al., 1971; Panofsky and Mazzola, 1971; Kaimal et al., 1976; Young, 1988; Angevine et al., 1994; Eng et al., 2003; Hogan et al., 2009; Ansmann et al., 2010; Lenschow et al., 2012). Typical fit functions of vertical σ_w^2 profiles are based on aircraft measurements provided by Lenschow et al. (1980) and Sorbjan (1986). With respect to point measurements of turbulence parameters, the vertical

*Corresponding author: Olga Kiseleva, Institute of Meteorology and Climate Research Troposphere Research (IMKTRO), Karlsruhe Institute of Technology (KIT), Hermann-von-Helmholtz-Platz 1, 76344 Eggenstein-Leopoldshafen, P.O. Box 3640, 76021 Karlsruhe, Germany, olga.kiseleva@kit.edu

wind speed variance parameter's representativity is a critical issue, too (e.g. MAHRT, 1998; STEINFELD et al., 2007). For example, HOGAN et al. (2009) found that variance profiles derived from lidar measurements at one particular site showed a case-to-case variability that was about as large as the scatter of fit functions provided by LENSCHOW et al. (1980) and SORBJAN (1986). Therefore, especially for complex terrain, aspects of uncertainty or representativity of point measurements can become quite relevant.

Cities located in valleys often suffer from poor air quality, as the exchange of heat, moisture, and air pollutants in the urban atmospheric boundary layer (UABL) and with the surroundings is limited by terrain effects (e.g., WANNER and HERTIG, 1984; MAYER, 1999; STEYN et al., 2013). This has been proven by different investigations. For example, RENDÓN et al. (2014) simulated how counteracting up-slope winds and country breezes can lead to poor urban ventilation during daytime. GIOVANNINI et al. (2017) reported that in the narrow and deep Adige valley, inhomogeneities in the urban areas modify the diurnal up- and down-valley winds considerably. ADLER et al. (2020) used horizontally scanning Doppler lidar measurements to show how blocking effects due to convergence of drainage flows from the main and a tributary river valley strongly reduce urban ventilation during nighttime.

To investigate the urban climate and provide recommendations for urban planning, high-resolution models on decametre scales are desirable. To foster and achieve these aims, a high-resolution urban climate and air quality model was developed (MARONGA et al., 2019; 2020), and comprehensive measurements for model evaluation were conducted (SCHERER et al., 2019b) within the framework of the project "Urban Climate Under Change [UC]²" (SCHERER et al., 2019a). The observations were carried out in cities under different environmental conditions (Berlin, Hamburg, Stuttgart). Stuttgart is a well-known example of a city located in hilly terrain suffering from frequent air quality issues which are related to its complex topography (MAYER, 1999; SCHERER et al., 2019a; REUTER and KAPP, 2021). At the same time, the area of Stuttgart is characterised by pronounced diurnal cycles of the meteorological and air-chemical parameters (KISELEVA et al., 2021; ZEEMAN et al., 2022; SAMAD et al., 2023).

While the practicability of the PALM-4U model for a user community was already tested (HALBIG et al., 2019; STEURI et al., 2020; WINKLER et al., 2020) and first applications were successfully carried out (e.g., GELETIČ et al., 2021), we aim to evaluate the PALM-4U model with respect to dynamical and turbulent parameters in the ABL. Special focus is given to the nocturnal wind field and the daytime σ_w^2. The paper is structured as follows. In Section 2, we describe the observations used for the model evaluation and the PALM-4U model setup. Section 3 provides the model evaluation of the simulated diurnal cycle of the wind in the convective (CBL) and nocturnal stably stratified boundary layers

(NBL) in the Stuttgart basin and Neckar valley. In Section 4, we focus on the model evaluation of σ_w^2 in the CBL. Finally, Section 5 summarises the main results of the investigation.

2 Observations, model setup, and analysis tools

2.1 Observations

The observations were performed over the orographically structured terrain characterising the surroundings of the city of Stuttgart in southwestern Germany (Figure 1a, b). Stuttgart is the sixth largest city in Germany with a population of about 630,000. The investigation area includes the relatively broad Neckar valley, oriented southeast to northwest (width about 2 km) and the basin-shaped valley referred to as Stuttgart basin (about 2.5 km x 2.5 km), which opens to the Neckar valley in the northeast (Figure 1b, c). The valley and basin floor are approximately at an altitude of 300 m above mean sea level (m asl) and surrounded by hills with ridge heights up to 520 m asl. The inner city of Stuttgart is located in a valley that extends from Kaltental in the southwest via the Stuttgart basin to the Neckar valley in the northeast of the city. The position of buildings (Figure 1c) and land use map (Figure 1d) show the high building density in the Stuttgart basin and somewhat lower building density in the lower parts of the surrounding hills. The sealed surfaces in the Neckar valley are often built with industrial facilities. The upper parts of the hills are mostly forested.

The topographic setting of Stuttgart strongly influences the meteorological situation in the city (SAMAD et al., 2023). While in the Neckar valley northwesterly and southeasterly winds predominate, the main wind direction within the Stuttgart basin is southwest or northeast. Nocturnal cold air flows from the hills supply the city with fresh air while upslope winds in the morning transport pollutants emitted in the city to the suburban areas and the outskirts.

Two intensive observation periods (IOPs) lasted from 05 July to 15 August 2017 and from 14 June to 31 August 2018. For a detailed overview of the measurement campaigns, we refer to SCHERER et al. (2019b). From these two summer periods, two episodes were selected for the PALM-4U evaluation, which were characterised by high pressure conditions and mainly clear skies. The first episode is from 14 to 15 August 2017 and the second is on 20 June 2018. During the two IOPs, different vertical profiling systems were operated (KISELEVA et al., 2019). An overview of instrumentation and measured parameters is given in Table 1. The measurement systems were operated differently in 2017 and 2018, according to the ABL parameters chosen for the PALM-4U evaluation, i.e., the horizontal wind field in 2017 and σ_w^2 in 2018. Their positions in the IOPs in the two years are shown in Figure 1b, c.

Meteorol. Z. (Contrib. Atm. Sci.)
Early Access Article, 2024

Olga Kiseleva et al.: Evaluation of the Urban Climate Model PALM-4U

3
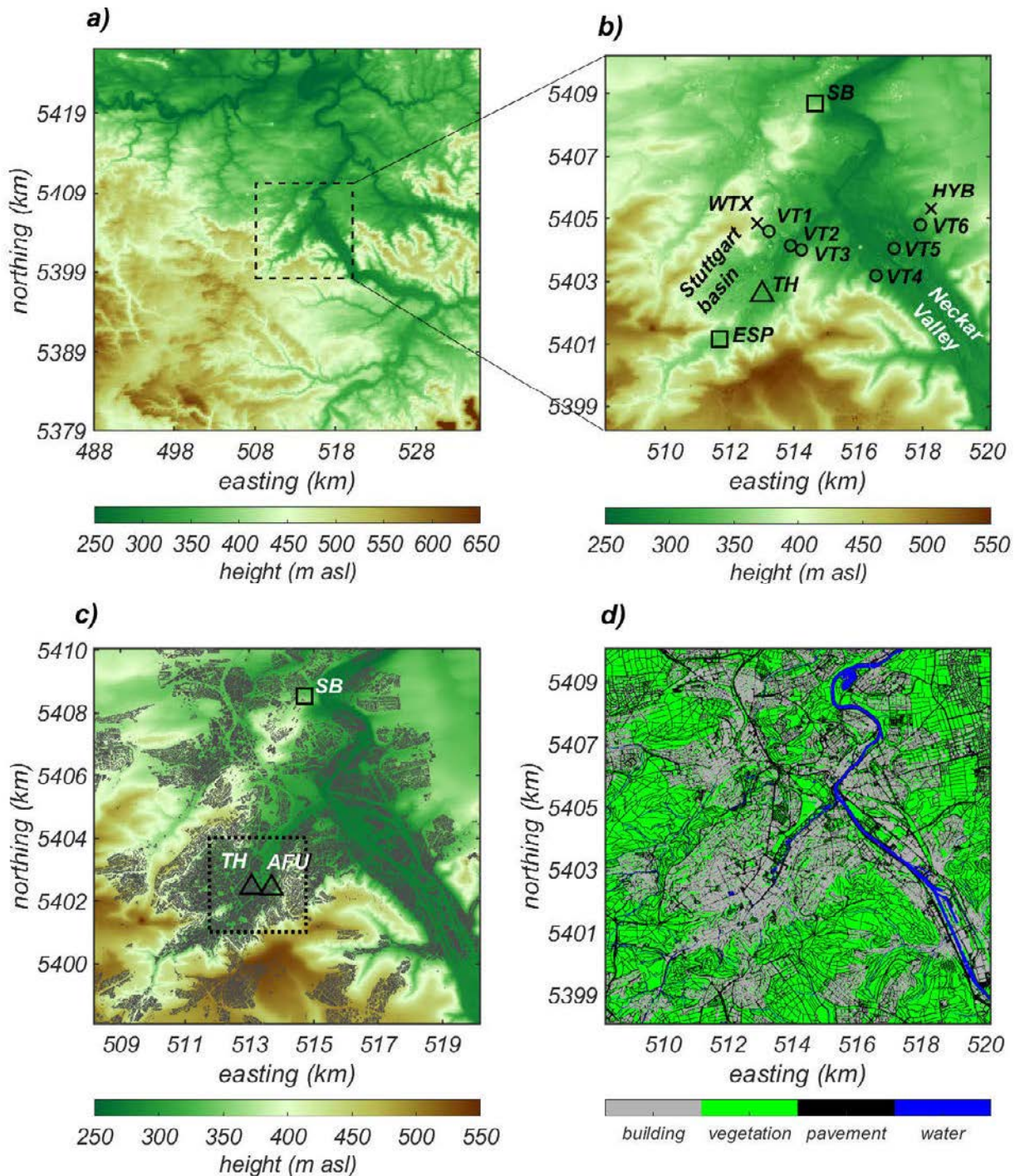
Figure 1: (a) The model domain with 40 m grid spacing for wind field evaluation on 14–15 August 2017 and (b) the location of observation sites Erwin-Schöttle-Platz (ESP), Town Hall (TH), Schnarrenberg (SB), lidars WTX and HYB, and corresponding virtual towers 1–6 (VT1, …, VT6). (c) Model domain with 10 m grid spacing for σ_w^2 evaluation on 20 June 2018 and location of observation sites (TH, SB, Amt für Umweltschutz (AFU)). Areas with buildings are grey shaded. 10-s output data are available for the 3 x 3 km² subdomain indicated by the dotted square. (d) land use distribution. The latitudinal and longitudinal coordinates of the southwestern corner in (a) are 48.562721° N, 8.838169° E. Topographic data is provided by DLR. Coordinate system: UTM (ETRS89) zone 32U, geoid egm2008.

The wind lidar of type Leosphere Windcube WLS8-3 was installed at the Town Hall (TH, wavelength of 1.543 µm, pulse energy of 200 µJ, pulse repetition frequency of 20 kHz). The wind lidar was operated in two modes: the Doppler beam swing (DBS) mode in 2017, and the vertical stare mode in 2018. Using the DBS mode, the wind lidar performed measurements of radial wind speeds with a cone angle of 14.84° along the four beam directions of 90, 180, 270, and 360°. It took the wind lidar 7 s to collect data at each beam location and to steer the beam to the next beam location. The 2-D wind components were derived with a vertical resolution of 20 m from 40 m up to a maximum of 600 m above the roof level (depending on the aerosol

Table 1: Region, station name and abbreviation, measurement platform and measured parameters for the IOPs in the two years 2017 and 2018. T is the temperature, p is the air pressure, RH is the relative humidity, w is the vertical wind speed, $|v|$ is the horizontal wind speed, wd is the wind direction, z_i is the boundary-layer height and CBH is the cloud-base height. The station height data are based on the coordinate system UTM (ETRS89) zone 32U, geoid egm2008. Site locations are indicated in Fig. 1b,c. *The weather station was approx. 200 m away from TH.

Region	Station name (elevation in m asl)	Abbreviation	Measurement platform	Measured meteorological parameters
Stuttgart basin	Town hall (303)	TH	Wind lidar Weather station*	$|v|$, wd (2017), w (2018) T, RH, $|v|$, wd
	Erwin-Schöttle-Platz (322)	ESP	Radiosonde Weather station	T, p, RH, $|v|$, wd (2017) T, RH, $|v|$, wd
	Amt für Umweltschutz (333)	AFU	Wind lidar	w (2018)
	Virtual tower 1 (316)	VT1		$|v|$, wd up to 500 m agl (2017)
	Virtual tower 2 (287)	VT2		$|v|$, wd up to 2000 m agl (2017)
	Virtual tower 3 (302)	VT3	Wind lidars	$|v|$, wd up to 500 m agl (2017)
Neckar valley	Virtual tower 4 (275)	VT4	Dual-Doppler scan pattern	$|v|$, wd up to 500 m agl (2017)
	Virtual tower 5 (278)	VT5		$|v|$, wd up to 2000 m agl (2017)
	Virtual tower 6 (301)	VT6		$|v|$, wd up to 500 m agl (2017)
	Schnarrenberg (366)	SB	Ceilometer	z_i, CBH (2017, 2018)
			Radiosonde	T, p, RH, $|v|$, wd (2017, 2018)
			Weather station	T (0.05 and 2 m agl), RH, $|v|$, wd

concentration) and with a temporal resolution of 10 min from instantaneous radial velocities measured at each beam position by the internal software provided by Leosphere. According to the manufacturer's technical specifications, the accuracy of the wind speed is 0.2 m s^{-1} and of wind direction is 1.5°. In summer 2018, the wind lidar was operated in vertical stare mode only. In this mode, the wind lidar beam was continuously pointing vertically, which provided a direct measurement of the vertical wind speed with a time resolution of 7 s. At TH, data from a weather station were available, too.

Two Doppler lidars (WTX, HYB) of the type "Wind-Tracer", manufactured by Lockheed Martin, were installed in summer 2017 (Figure 1b) to derive wind profiles at 6 different sites (VT1, …, VT6) based on the virtual tower (VT) technique (e.g., WITTKAMP et al., 2021). Detailed technical information and settings of the two lidars are described by RÖHNER and TRÄUMNER (2013) and DAMIAN et al. (2014). For both devices, the range gate length was set to 69.5 m and the accumulation frequency was 10 Hz. The measurement range of the devices was 350 m to 12 km, depending on the atmospheric conditions. Both lidars are equipped with a freely configurable two-axis scanner. The manufacturer's software allows to perform highly synchronised scans with the two devices, which is required for the VT technique. The two lidar devices performed temporally synchronised scans, measuring simultaneously for 10 s at every measurement height of each VT. In total, 68 heights were scanned, and it took the two lidar devices approximately 15 min to complete one scan cycle.

On the roof of the Amt für Umweltschutz (AFU, Figure 1c) the wind lidar Streamline (Halo Photonics) was deployed in summer 2018. The height of the sensor was 332.6 m asl, around 21.5 m above ground level (agl). It was operated in vertical stare mode for vertical wind speed observations. The range gate length of the lidar was set to 18 m while the temporal sampling frequency was set to approximately 1 Hz; 15000 pulses were integrated into one such sample. The Doppler velocity resolution is specified by the manufacturer as 3.82 cm s^{-1}.

At Erwin-Schöttle-Platz (ESP), a radiosonde was launched at 1203, 1524, 1941, 2257 Universal Standard Time (UTC) on 14 August and at 0300, 0755, 1049 UTC on 15 August 2017 (Figure 1b). The Vaisala Radiosondes RS92 provided vertical profiles of pressure, temperature, relative humidity and wind speed, and direction with a vertical resolution of 5 to 10 m, depending on the ascent speed of the balloon. At ESP, also a weather station was operated.

At Schnarrenberg (SB), the Vaisala radiosonde systems RS92 (2017) and RS41 (2018) were operated (Figure 1b, c). Operational radiosoundings were available from different times of the day reaching up to about 32 km asl with a vertical resolution of about 10 m, providing profiles of air temperature, relative humidity, wind speed, wind direction, and air pressure. Routinely, the balloon was launched approximately 75 min before 0000 and 1200 UTC, that is at 2245 and 1045 UTC, respectively. For the 2017-episode, additional radiosondes were started 75 min before 0600 and 1800 UTC, that is at 0445 and 1645 UTC. For the RS92 and RS41 radiosonde systems, uncertainty of wind speed is 0.15 m s^{-1} and of wind direction 2°, and the total accuracy of temperature in the ABL is <0.5 K.

At SB, a ceilometer CHM15k Nimbus (manufactured by Lufft, wavelength of 1.064 μm, pulse energy of 7–8 μJ, repetition frequency of 5–7 kHz, MARTUCCI et al. (2010)) was running routinely. The CHM15k

Meteorol. Z. (Contrib. Atm. Sci.)
Early Access Article, 2024

Olga Kiseleva et al.: Evaluation of the Urban Climate Model PALM-4U

5

ceilometer is a lidar-based sensor that is used for cloud-base height and ABL height detection. The system provides profiles of uncalibrated backscatter up to 15 km agl with a range resolution of 5 m and a time resolution of 15 s. From these profiles, up to three cloud-base heights were determined based on a threshold method of the Lufft algorithm. Ceilometer intercomparisons by MARTUCCI et al. (2010) and MILROY et al. (2012) provide an accuracy of cloud-height detection of about 150 m. We used only the lowest cloud-base height. Finally, at SB a weather station provided near-surface data.

2.2 PALM-4U model setup

The large-eddy simulation (LES) model PALM-4U was designed to allow high-resolution simulations (metres to decametres) over urban areas. A detailed description is given by MARONGA et al. (2019, 2020). Therefore, we confine ourselves to the configuration of PALM-4U used in this study. We applied PALM release 21.10 driven with COSMO analysis data. The synthetic turbulence generator implemented in PALM-4U is turned on to adjust the turbulence conditions at the inflow (KADASCH et al., 2021). The method is based on the work of XIE and CASTRO (2008) and KIM et al. (2013).

The simulations were initialised using three input files, the namelist, static (static driver) and dynamic input files (dynamic driver). The static driver contains all static information to initialise land- and urban-type surfaces, such as topography, geographical coordinates, surface, vegetation, and building information. This information was provided by Deutsches Zentrum für Luft- und Raumfahrt (DLR), supplemented by OpenStreetMaps data prepared by module A of (UC)2 (SCHERER et al., 2019a; HELDENS et al., 2020). The used terrain data are based on the coordinate system UTM (ETRS89) zone 32U, geoid egm2008. Terrain height in this coordinate system differs by approximately 50 m from German governmental terrain height data. The dynamic driver contains the information on the initial state of the meteorological fields (such as 3-D data of wind, temperature, humidity, pressure, soil moisture, soil temperature) as well as the boundary data required for the offline nesting of PALM-4U. These are interpolated from 1-h output data of the model COSMO (SCHÄTTLER et al., 2014) using the pre-processing tool INIFOR. For soil- and wall-layer temperature, a spin-up phase of 24 hours was used before the start of the atmospheric model. As the format of the standard COSMO analysis changed from COSMO-DE to COSMO-D2 in May 2018 (with reduction in grid spacing from 2.8 km to 2.2 km and increase in the number of vertical levels from 50 to 65), we used COSMO-DE data for the 2017 simulations (Sec. 3) and COSMO-D2 data for the 2018 simulations (Sec. 4).

As it turned out that the influence of the upstream topography of the Neckar valley is stronger for nocturnal flow fields in the investigation area than its influence on the daytime convection in the Stuttgart basin, the model domains were chosen differently for the two evaluation periods. The PALM-4U model domain for the wind field evaluation (Sec. 3) and for the turbulence evaluation (Sec. 4) are shown in Figure 1.

On 14–15 August 2017, the model size was 48 x 48 x 4 km^3 in x-, y-, and z-direction (Figure 1a), respectively, and the isotropic grid spacing was 40 m. We started the model on 13 August 2017 at 2100 UTC with the simulation time of 39 h. The model evaluation covers the period from 0000 UTC on 14 August to 1200 UTC on 15 August. The instantaneous 3-D volume output of temperature (T), specific humidity (q), and u-, v-, and w-wind components was every 10 min. Additionally, we stored height-resolved u,v,w data (1 s) at VT2 up to 400 m agl to allow TKE calculation.

On 20 June 2018, a model domain size of 12 km × 12 km × 2.5 km^3 in x-, y- and z-directions (Figure 1c), respectively, with an isotropic grid spacing of 10 m was used. The start time of the simulation was set to 20 June 2018 at 0000 UTC and the simulation time was 18 h. The model evaluation then includes the period from 0900 to 1800 UTC on 20 June. The instantaneous 3-D volume data of u, v, w-components of the velocity, T, q, and potential temperature (Θ) were stored every 15 min. Additionally, we stored height-resolved vertical wind speed (10 s) for two boxes of 100 x 100 x 2500 m^3 around each of two evaluation sites TH and AFU (Figure 1c), and for a 3 x 3 km^2 subdomain at the level of 350 m agl (Figure 1c).

2.3 Analysis tools

2.3.1 Atmospheric boundary-layer height

We assume a CBL to be existing when the near-surface layer is unstably stratified. The SB station provides the vertical temperature gradient for the layer 2 m above ground. Concerning radiosoundings, we applied the parcel method, the maximum gradient method using Θ and specific humidity profiles as well as the bulk Richardson number (Ri) method to determine z_i (e.g., ADLER et al., 2019). We applied sensitivity tests to the three methods. The maximum gradient method proved to be most robust because it does not depend on the exact value of the surface air temperature as does the parcel method. Therefore, their results were used in the following. To determine z_i from the model simulations, we applied the parcel method to Θ profiles. As 10 and 40 m vertical resolutions were used in the simulations, we also compared the impact on the z_i determination. No considerable differences were found. In Section 3, we used the Θ profiles from locations SB und ESP. In Section 4, the mean Θ profiles, that were calculated from hourly outputs over a 3 x 3 km^2 area (Figure 1c), were used. The standard deviations of these mean profiles were applied to determine the statistical uncertainty of z_i.

The top of the NBL can be defined as the transition between the stable surface layer and the neutral residual layer (STULL, 1988). This height was detected by scanning the temperature gradient profile of radiosonde observations and model output upwards to
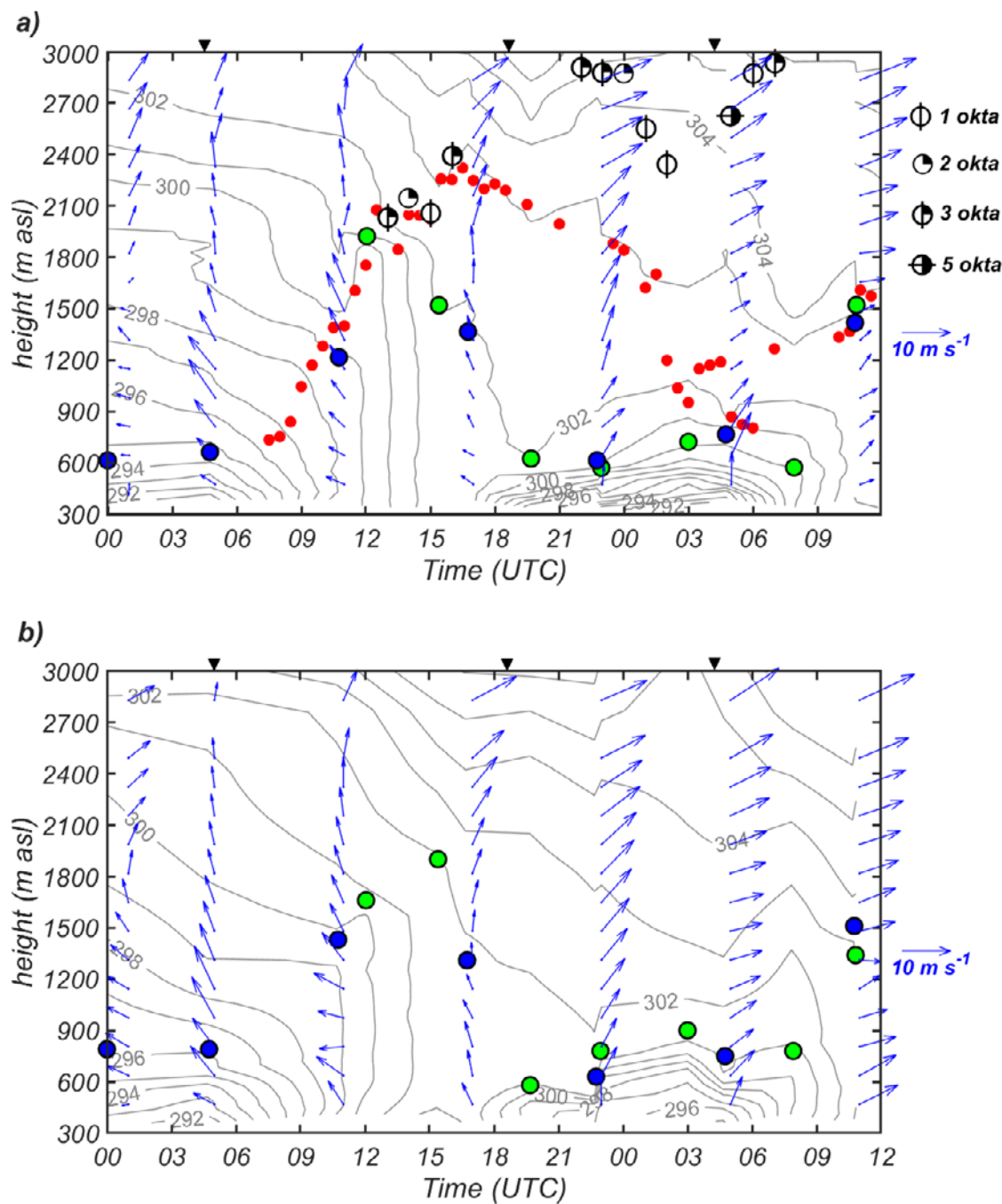
Figure 2: Time-height sections of Θ (isolines), horizontal wind speed (arrows), boundary-layer characteristics (CBL, NBL, and RL), and clouds for 14 August 0000 UTC to 15 August 1200 UTC. (a) Potential temperature and horizontal wind speed are based on the radiosoundings of SB. blue dots: radiosonde at SB, green dots: radiosonde at ESP, red circles: ceilometer at SB. Cloud base and cloud coverage (in oktas) are based on ceilometer data from SB. The triangles indicate (left to right) the sunrise, sunset, and again sunrise. The site locations of the different observation systems are given in Figure 1b. (b) same as in (a) but from the PALM-4U simulations. The blue and green dots indicate CBL and NBL height at SB and ESP, respectively.

find the lowest level at which the Θ gradient, dΘ/dz, reaches its minimum and then checking if at that level, the following condition is met: $|d^2\Theta/dz^2| < 0.1$ K^2 km^{-2}. Figure 2 shows the detection of CBL and NBL heights based on these introduced algorithms.

The manufacture's software of the ceilometer deployed at SB provides three levels with significant vertical changes in attenuated backscatter (threshold method, e.g., Babić et al., 2019; Ritter and Münkel, 2021; Kotthaus et al., 2023). We used the lowest

level for z_i detection, i.e. for CBL or NBL top when the near-surface layer is unstable or stable, respectively. Hourly mean and standard deviation of z_i were calculated from 15 s ceilometer measurements.

2.3.2 Horizontal wind

We used measured profiles of horizontal wind from two different kinds of systems (Tab. 1): wind lidar (TH, VTs) and radiosondes (SB, ESP). The observations

Meteorol. Z. (Contrib. Atm. Sci.)
Early Access Article, 2024

Olga Kiseleva et al.: Evaluation of the Urban Climate Model PALM-4U

7

from the systems were available with different temporal resolutions (Sec. 2.1). For evaluation of the PALM-4U simulations, wind-lidar observations and model output were aggregated to hourly means.

2.3.3 Variance of the vertical wind speed

The wind lidar and simulation data were used to calculate σ_w^2. The values were computed for 1-h and 3-h intervals. To ensure a good data quality of the lidar data, a two-step procedure was applied: values with a carrier-to-noise ratio (CNR) lower than 27 dB (Windcube WLS8-3) and 19.0 dB (Halo Photonics) were discarded, and range gates with data availability of more than 75% within 1 h only were considered.

As the observation and simulation data have different temporal sampling rates (Windcube WLS8-3: 7 s, Halo Photonics: 1 s, simulations: 10 s), a high-pass filter with a frequency of 0.10 Hz was applied to the observation data. This also helped to remove random uncorrelated noise automatically. The results of this method were compared to the established methods of LENSCHOW and KRISTENSEN (1985) and LENSCHOW et al. (2000), i.e. the estimation of random uncorrelated noise by extrapolating the autocorrelation function of the variance to the zero lag. The outcome was quite similar, with differences amounting to $\approx$ 1–1.5%.

3 Model evaluation of the wind field in the boundary layer

The synoptic conditions during the two-day period from 14 to 15 August 2017 were dominated by a high-pressure system centred over eastern Europe and an eastward propagating low-pressure system with its centre over Scotland. On 14 August, this was associated with weak free-tropospheric wind from the southeast, which turned to southwest in the evening (Figure 2a). On 15 August, south-westerly wind prevailed throughout the day. Both days were generally characterised by fair weather conditions and were mostly cloudless with only few cumuli topping the CBL during daytime, as visible in the measurements of global radiation (not shown) and ceilometer backscatter at SB (Figure 2a). These synoptic flow conditions were well represented in the PALM-4U simulations (Figure 2b).

3.1 Boundary-layer conditions

The Θ profiles in the ABL from radiosoundings show that a moderately stably stratified NBL up to about 600 m asl existed in the night of 14 August (Figure 2a). After sunrise, the CBL deepened continuously, reaching about 2000 m asl at 1200 UTC. While the determination of the depth of the growing CBL agrees between radiosounding and ceilometer backscatter data, the CBL depth estimation in the afternoon (after about

1500 UTC) differed considerably. We assume that the backscatter data indicated the height of the residual layer (RL), while the decrease of the CBL based on the radiosounding data is due to warm-air advection associated with the approach of the low-pressure system. An NBL started to form around sunset at about 1800 UTC, then grew in depth and strength throughout the night and reached up to around 700 m asl at 0300 UTC on 15 August 2017. By this time, a strong surface inversion with a vertical potential temperature gradient of 2.25 K $(100 \text{ m})^{-1}$ was visible in the radiosounding data. After about 0700 UTC, Θ increased in the NBL due to surface heating, and the developing CBL eroded the NBL from below. By around 1100 UTC, a CBL had developed and reached up to 1500 m asl.

Figure 2b provides the evolution of Θ and ABL from the PALM-4U simulation. Due to the observed small number of cumuli (Figure 2a), we neglected clouds in the simulation. The comparison shows that the main thermodynamic conditions are well represented by the simulation: the weaker but deeper NBL in the first night, a CBL depth of about 2000 m asl on 14 August, and a strong and shallow NBL on the night from 14 to 15 August, although somewhat weaker in the simulations than in the observations. This means that the preconditions for the evaluation of PALM-4U concerning the flow field in the ABL were given.

3.2 The diurnal cycle of the wind field

For comparison of the simulated wind with the observations, we focused on characteristic levels with respect to the ABL. The first level was chosen at 1000 m asl ($\approx$ 700 m agl) to be approximately in the middle of the daytime CBL (Figure 2) and the second was chosen at 410 m asl ($\approx$ 100 m agl) to be within the NBL during the night. Vertical profiles of wind speed and wind direction at ESP, TH, and VT2 in the Stuttgart basin and at SB and VT5 in the Neckar valley are available for the comparison. The diagrams include instantaneous values from the radiosoundings at ESP and SB, 1-h means including standard deviations from the virtual lidar measurements at VT2 and VT5, calculated from 15-min resolution measurement data (Sec. 2.1), and 1-h means and standard deviations from the simulations, calculated from 10-min resolution output (Sec. 2.2).

The observed flow conditions in the investigation area at 1000 m asl could be separated into three main periods (Figure 3): 0000 to 0900 UTC on 14 August, when wind speeds of up to 8 m s^{-1} occurred blowing from south-easterly directions. The second time interval covers approximately the period from 0900 to 2100 UTC on 14 August. During this period, the wind speed reduced to 3–4 m s^{-1} while the wind direction turned to south-westerly directions at the end of the time interval. The third time interval covers the night from 14 to 15 August and the first half of 15 August. During this period, the wind speed reached up to 8–10 m s^{-1} while the wind direction was still from the southwest. In general, the
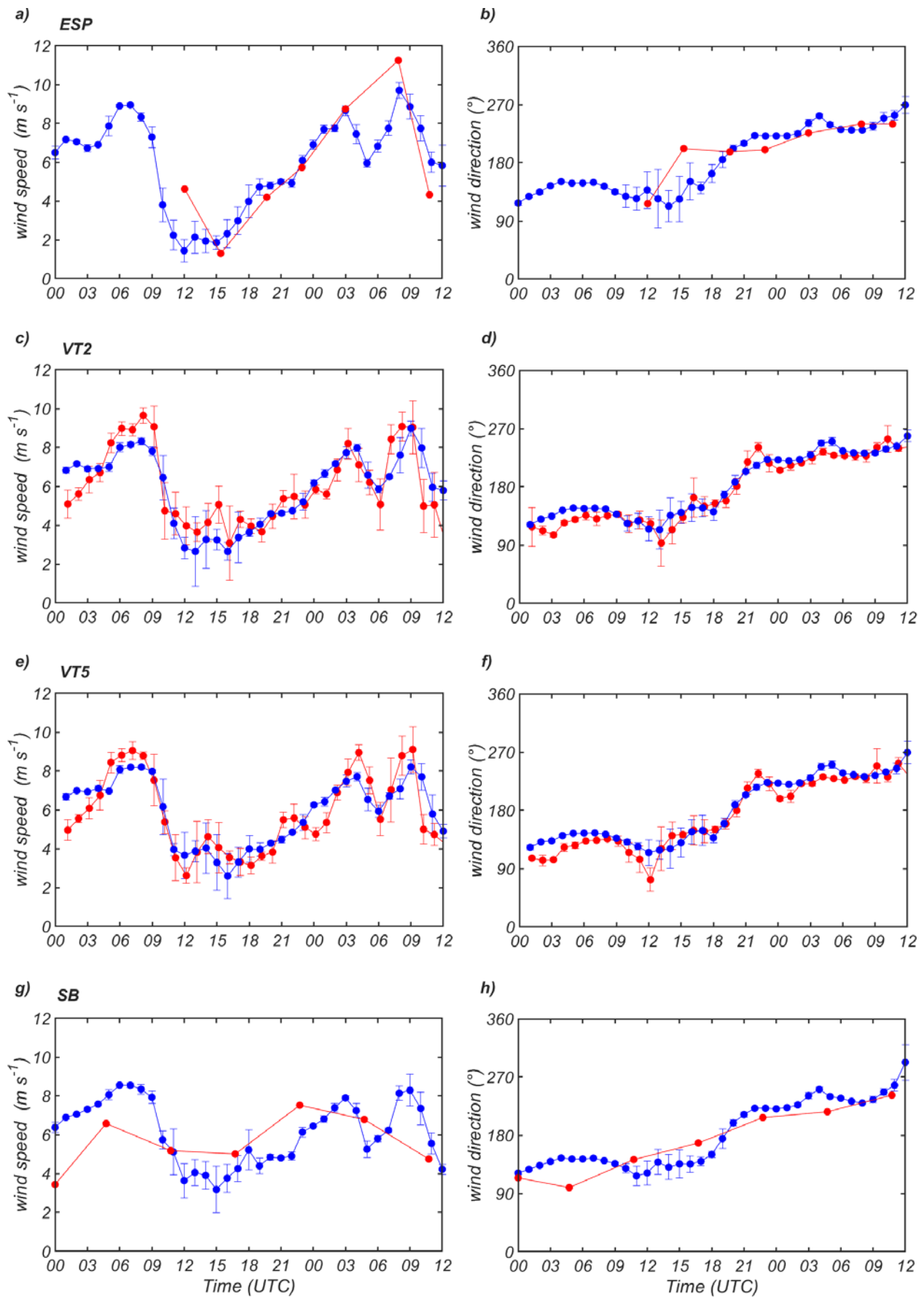
Figure 3: Hourly means and standard deviation of the wind speed and direction from lidar or instantaneous data from radiosoundings (red) at 1000 m asl (700 m agl) at ESP (a,b) VT2, (c,d), VT5 (e,f), and SB (g,h) for 14 August 0000 UTC to 15 August 1200 UTC. The site locations of the observation sites are shown in Figure 1b. The corresponding model results are given in blue.

Meteorol. Z. (Contrib. Atm. Sci.)
Early Access Article, 2024

Olga Kiseleva et al.: Evaluation of the Urban Climate Model PALM-4U

9
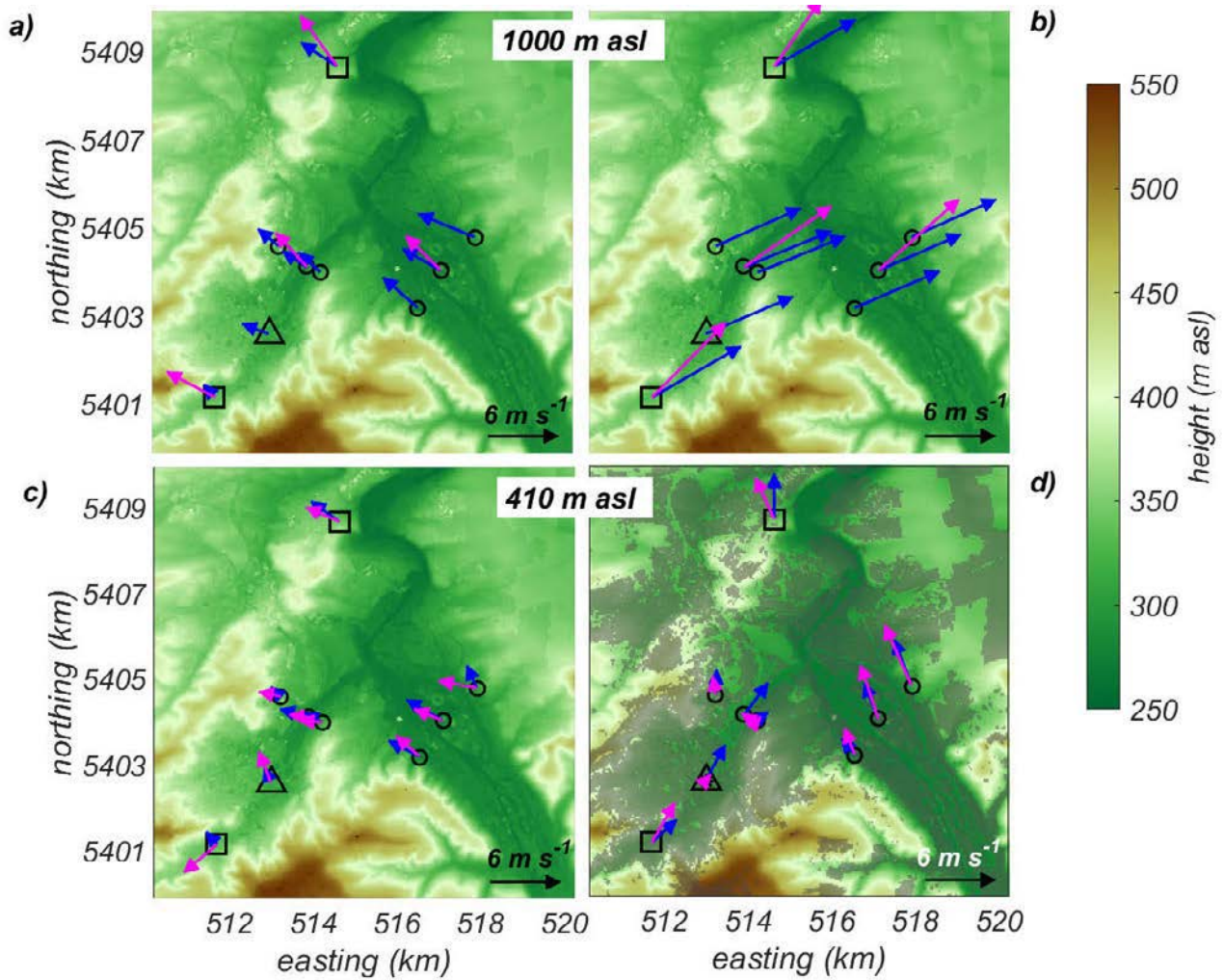
Figure 4: Hourly averaged measured (magenta) and simulated (blue) wind vectors (a,c) from 1200–1300 UTC on 14 August and (b,d) from 0300–0400 UTC on 15 August at two levels. Squares indicate radiosonde stations, circles virtual towers and the triangle the lidar site. In (d) the areas with buildings (grey shaded) are added. Station names see Figure 1b.

simulated wind conditions show a good agreement with the measurements both in the Stuttgart basin and in the Neckar valley. The standard deviations of the measured and simulated wind speed and wind direction overlap quite often throughout the day. The diagrams also show that the simulations sometimes differ more from the instantaneous radiosounding values than from the temporally averaged wind lidar data. Figure 4a, b visualises the spatial flow fields at 1000 m asl for representative daytime (1200–1300 UTC on 14 August) and nighttime periods (0300–0400 UTC on 15 August). Particularly the spatially homogeneous flow fields that exist during both periods become clearly visible as well as the good agreement between observations and simulation.

To quantify the differences between measurements and simulation, we calculated root mean square error (RMSE) and normalised RMSE (NRMSE) from the measured and simulated time series. The results are summarised in Table 2a. The RMSE values vary between 1.0 and 1.5 m s^{-1} which, with respect to the mean wind speed of 5 m s^{-1} at that level, results in NRMSE values between 0.2 and 0.3.

Figure 5 presents the temporal development of the wind at 410 m asl (100 m agl). In the Stuttgart basin, the measured wind was quite low in the NBL on the first night (<2 m s^{-1}, Figure 5a, c, e) and a pronounced down-valley wind did not develop at 100 m agl (Figure 5b, d, f; the dashed line indicates the orientation of down-valley wind direction). Between 0800 and 0900 UTC, as the CBL started to grow (Figure 2a) and momentum was mixed downward, the wind speed at all sites in the Stuttgart basin increased to values of 2–4 m s^{-1} (Figure 5a, c, e). Note that the south-easterly wind prevailing between 0900 and 1800 UTC does not correspond to the up-valley wind direction of the Stuttgart basin but corresponds to the wind direction at 1000 m asl (Figure 3b, d) so that we assume that vertical coupling between the flow layers of the CBL exists. Then, between 1800 and 2100 UTC, a south-westerly down-valley wind established in the Stuttgart basin (Figure 5b, d, f). As the large-scale wind also turned to southwest during that time interval (Figs. 2a, 3), it is hard to decide whether this flow is a thermally-driven down-valley wind accompanied by a decoupling of the
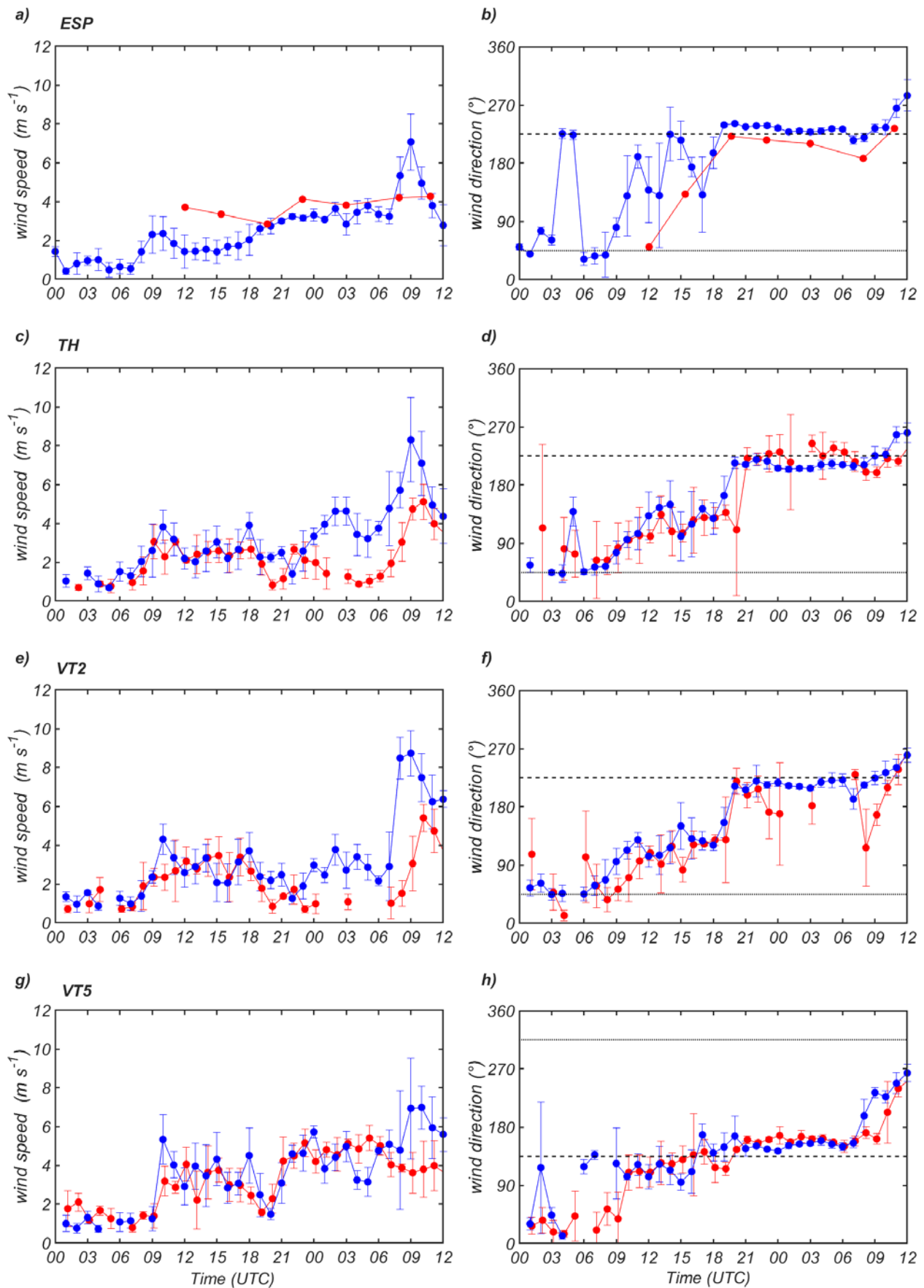
Figure 5: Hourly means and standard deviation of the wind speed land direction from lidar or instantaneous data from radiosoundings (red) at 410 m asl (100 m agl) at ESP (a,b), TH (c,d), VT2 (e,f), VT5 (g,h), and SB (i,j) for 14 August 0000 UTC to 15 August 1200 UTC (site locations of the measurements see Figure 1b). The dotted line indicates the up-valley and the dashed line the down-valley direction of the Stuttgart basin and Neckar valley, respectively. The corresponding model results are given in blue.

Meteorol. Z. (Contrib. Atm. Sci.)
Early Access Article, 2024

Olga Kiseleva et al.: Evaluation of the Urban Climate Model PALM-4U

11
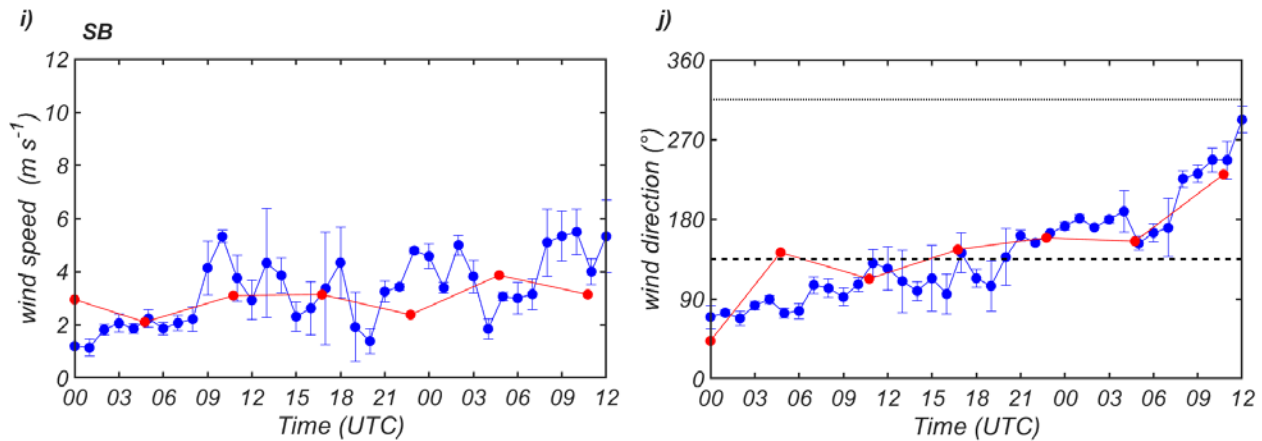
Figure 5: (Continued)

flow in the NBL from the one in the RL or if the flow in the NBL and in the RL are still coupled. However, Ri (Eq. 1, see Sec. 3.3), calculated for the lowest 500-m layer at nighttime, results in Ri > 1 and suggests a decoupling of the flow in the NBL from the one in the RL. Both features, vertical coupling during the day and decoupling at night of flows in the ABL in the Stuttgart area were reported by WITTKAMP et al. (2021). After 0700 UTC on 15 August, the wind speed in the Stuttgart basin increased moderately to values of 4–5 m s^{-1} (Figure 5a, c, e) while the wind direction remained southwest.

Considering the simulation results for the Stuttgart basin, the observed wind speed (Figure 5a, c, e) and wind direction (Figure 5b, d, f) at 100 m agl are well reproduced until 2100 UTC on 14 August: no down-valley flow at TH and VT2 was simulated (Figure 5d, f) in the first night as well as the increase in the wind speed and the turning of the wind direction from northeast to southeast in the morning was captured by the model. However, at ESP a weak down-valley flow between 0400 and 0500 UTC on 14 August was simulated (Figure 5a, b). This will be investigated later by looking at weather station data, as radiosoundings were not available at ESP during this period. The occurrence of the measured down-valley wind after 2100 UTC on 14 August was also correctly simulated. However, pronounced differences in wind speed become visible in the night and particularly in the morning of 15 August. For example, while the observed wind at TH was low during the night (< 2 m s^{-1}) the modelled wind speed reached up to 4 m s^{-1} (Figure 5c). Somewhat less pronounced deviations exist between measurement and simulation at VT2 during the night (Figure 5e). Finally, after about 0700 UTC on 15 August, the simulated wind speed increases to about 8 m s^{-1} while the measured values are on average lower than 6 m s^{-1} (Figure 5a, c, e).

To clarify whether a shallow down-valley flow had developed in the Stuttgart basin during the first night, as indicated by the simulation for ESP at 100 m agl between 0400 and 0500 UTC (Figure 5b), we analysed the simulation data of ESP and TH (40 m agl) and the corresponding weather station data at ESP (10 m agl) and observations very close to TH (city centre, 25 m agl). At both sites, a weak down-valley flow (< 1 m s^{-1}) was observed and simulated however, more intermittent, during the night until 0600 UTC (not shown). A similar depth of the down-valley flow (approximately 100 m agl) in the Stuttgart basin under comparable weather conditions was also reported by BAUMBACH et al. (1999).

In the Neckar valley at VT5 and SB, the wind speed in the NBL was also quite low during the first night (≤ 2 m s^{-1}, Figure 5g, i) coming from easterly or north-easterly directions (Figure 5h, j). At around 0900 UTC, the wind direction changed to southeast and the wind speed rose to values of about 4 m s^{-1}. Between 1800 and 2100 UTC, another slight increase in wind speed occurred while the south-easterly down-valley wind remained. All temporal behaviour of wind speed and wind direction is adequately reproduced by the model simulations (Figure 5g–j). Only, as already observed for the Stuttgart basin, the simulations overestimate the wind speed after 0900 UTC on 15 August (Figure 5g, i).

The spatial distribution of the flow field at 410 m asl during day- and nighttime is shown in Figure 4c, d. The flow fields of the daytime hours again demonstrate the strong vertical coupling of the layers in the CBL while the nocturnal flow fields indicate the decoupling particularly visible for the Neckar valley (VT4, VT5, VT6, SB). It also shows the section of the Stuttgart basin (TH, VT1, VT2, VT3) where considerable differences between the simulated and the measured wind speed occur during the night.

In the Stuttgart basin, the RMSE of wind speed at 410 m asl for the whole 36-h period is 1.6 m s^{-1} at TH and even 2.0 m s^{-1} at VT2 and ESP (Tab. 2). As the mean wind speed is only slightly higher than 2 m s^{-1}, e.g., the NRMSE reaches up to 0.9 at VT2. Concerning the wind direction, RMSE is about 35°. Since major differences between observed and simulated winds in

Table 2: RMSE and NRMSE of the horizontal wind speed and RMSE for wind direction between observations and PALM-4U simulations for (a) 1000 m asl and (b) 410 m asl for the sites TH (only available for 410 m asl), ESP, and VT2 in the Stuttgart basin and SB and VT5 in the Neckar valley. The locations of the different sites are indicated in Fig. 1b. Values without brackets are for 0000 UTC on 14 August to 1200 UTC on 15 August while values in brackets are for the 0000 to 2100 UTC on 14 August.

a)

1000 m asl (700 m agl)

	wind speed		wind direction
	RMSE (m s⁻¹)	NRMSE (-)	RMSE (°)
ESP	1.5	0.3	52.4
VT2	1.2	0.2	13.6
SB	1.3	0.3	15.3
VT5	1.0	0.2	16.0

b)

410 m asl (100 m agl)

	wind speed		wind direction
	RMSE (m s⁻¹)	NRMSE (-)	RMSE (°)
TH	1.6 (0.7)	0.8 (0.4)	29.6 (34.8)
ESP	2.0	0.5	39.0
VT2	2.0 (0.8)	0.9 (0.4)	35.4 (31.3)
SB	1.3	0.5	32.4
VT5	1.4 (1.1)	0.4 (0.5)	35.2 (43.0)

the Stuttgart basin occur during the night and morning hours of 15 August, we additionally calculated RMSE and NRMSE on the subset of data available until 2100 UTC of 14 August (only for TH and VT2 because for the radiosonde stations the limited number of soundings does not allow meaningful statistics). The much better coincidence between the measurement and simulation during this reduced period is reflected in a more than halving of RMSE for the wind speed while the wind direction is nearly unaffected by the reduced time period. Possible reasons for the major differences between the measurements and simulations of the period after 2100 UTC will be investigated in Section 3.3.

In the Neckar valley, the RMSE values for the 36-h period are 1.3–1.4 m s⁻¹, i.e. somewhat lower compared to the Stuttgart basin. The differences between the Stuttgart basin and the Neckar valley become more obvious when the NRMSE are compared. The NRMSE values are about 0.4–0.5 and even independent from the considered time period. The low NRMSE values are caused by the fact that a pronounced down-valley wind became established in the Neckar valley in the night from 14 to 15 August (Figs. 4, d and 5h, j). Concerning the wind direction, the RMSE is about 35°, which is similar to the one in the Stuttgart basin. Considering that the angle between the Stuttgart basin and the Neckar valley is about 90°, an RMSE of 35° indicates that the simulation clearly distinguishes between flows in the Stuttgart basin and Neckar valley.

3.3 Discussion of possible reasons for differences between measured and simulated wind

As outlined in the previous section, the simulated wind speed was higher than measured in the Stuttgart basin at 410 m asl during the night from 14 to 15 August (Figure 5c, e) and in the morning of 15 August (Figure 5a, c, e). Figure 6 shows the simulated and measured wind speed profiles under the nighttime and morning conditions of 15 August. A nocturnal low-level jet (LLJ) developed in the area of interest (Figure 6a). While the wind speed at the height of the LLJ wind speed maximum does not differ considerably between simulation and observations ($\approx$ 11 m s⁻¹ in the simulation and $\approx$ 9 m s⁻¹ in the observations), the LLJ in the simulation is at $\approx$ 700 m agl while the observed one is at $\approx$ 900 m agl. Additionally, the NBL is slightly more stably stratified in the observation than in the simulation (Figure 2).

We calculated the bulk Richardson number Ri, to investigate the nocturnal period in more detail:

$$Ri = \frac{g \Delta z}{\Theta_0} \frac{\Delta \Theta}{(\Delta |v|)^2} \qquad (3.1)$$

where Θ_0 is near-surface potential temperature, g is gravitational acceleration, Δz is the height of a reference level, $\Delta \Theta$ and $\Delta |v|$ are the differences of potential temperature respectively absolute value of wind speed between the reference level and the surface. We determined the nighttime Ri values for the layer between the height of the LLJ wind speed maximum and the surface. The Ri values based on the observed nocturnal conditions in the Stuttgart basin range from 1.6–4.4 while the simulated values range from 0.0–0.4 only. This means that Ri from observations indicate suppression of vertical turbulent mixing, while Ri values from the simulation, which are close to the critical Richardson number of 0.25, indicate that shear-generated turbulence allows transport of momentum from the LLJ layer downwards. The impact of LLJs on turbulence beneath the jet and on near-surface wind was already emphasised e.g. by Corsmeier et al. (1997), Banta et al. (2003), and Kiseleva et al. (2021). Figure 6c shows the simulated turbulent kinetic energy (TKE) determined for 15 min intervals and based on 1-s output at VT2. Enhanced TKE values of up to 0.5 m²s⁻² below the LLJ level are noticeable in Figure 6c and support the assumption that probably an unrealistic occurrence of vertical turbulent mixing was simulated by PALM-4U and was responsible for the larger simulated than measured wind speed at 410 m asl at night. Another reason for the higher wind speed at 410 m agl in the simulations than in the observations could also be that a vertical resolution of 40 m could be insufficient to simulate the NBL because the turbulence is not resolved properly. By this, the sub-grid scale turbulence scheme could cause a too strong
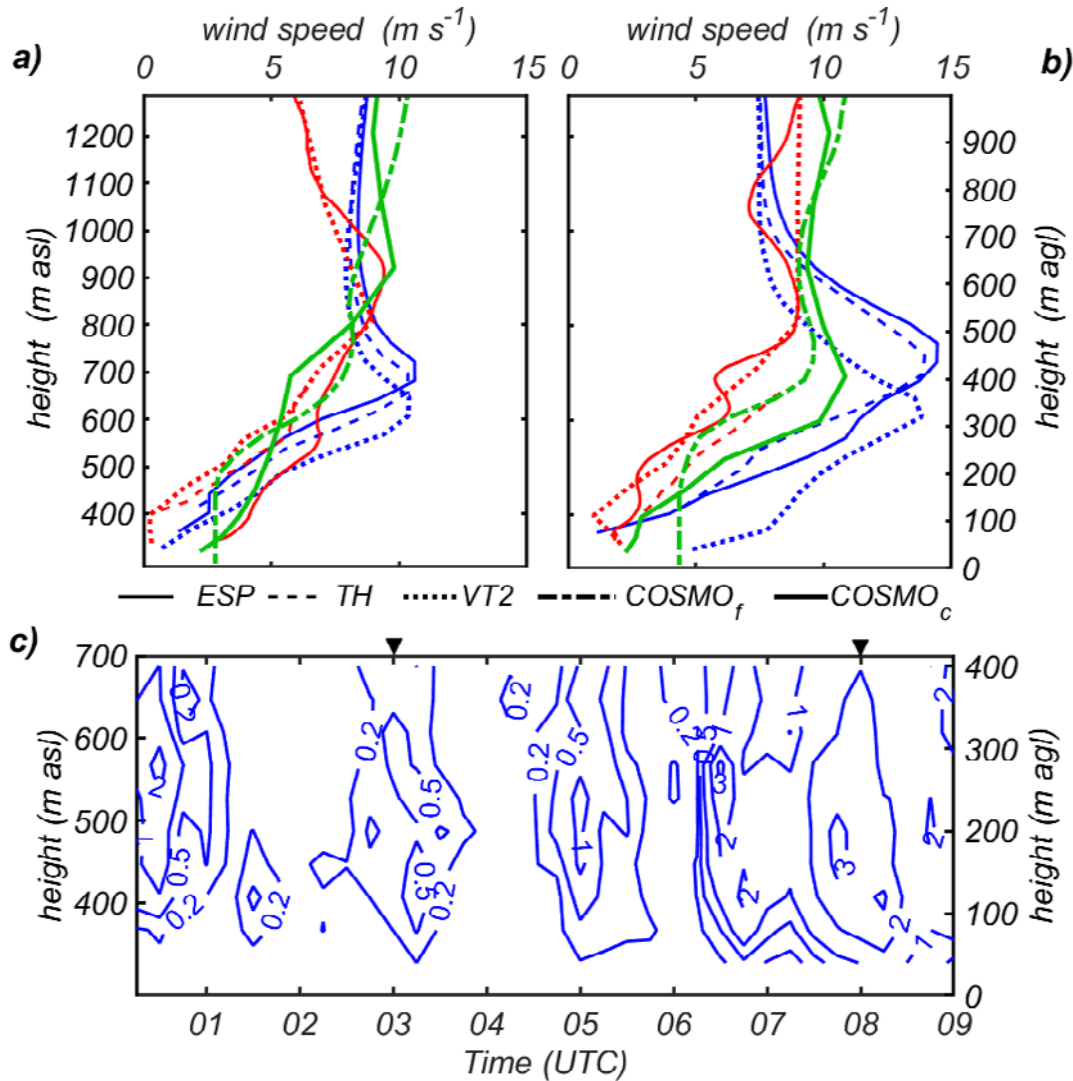
Figure 6: (a) Profiles of wind speed at ESP, TH, and VT2 at 0300 UTC on 15 August. Measurements in red and PALM-4U simulations in blue. COSMO DE profiles of the corresponding grid box in the Stuttgart basin (COSMOc) and at the southwestern boundary of the PALM-4U model domain (COSMOf) are shown in green. (b) The same but for 0800 UTC on 15 August. (c) Time-height cross section of simulated TKE at VT2 from 0000 to 0900 UTC on 15 August. The triangles indicate 0300 and 0800 UTC.

turbulent mixing (van Stratum and Stevens, 2015). Unfortunately, due to the scanning procedure (Sec. 2.1), TKE with good statistics cannot be determined from the lidar observations for comparison with model results.

The larger simulated than observed LLJ strength in the morning of 15 August (Figure 6b) could be responsible for the corresponding differences of the wind speed at 410 m asl (Figure 5). Although the unstable atmospheric conditions (Figure 2) allow vertical mixing beneath the LLJ in the simulations and observations alike ($Ri < 0.25$), the simulated jet velocity of up to 14 m s^{-1} represents a stronger source for turbulent downward transport of momentum from the LLJ level and large TKE values (≈ 3 m^{2}s^{-2}, Figure 6c) compared to the observed jet velocity < 10 m s^{-1} (Figure 6b).

To explain the differences between the simulated and observed LLJ characteristics, i.e. simulated too low during the night and too low and too strong in the morning, we investigated the impact of the driving COSMO model on the PALM-4U simulations. For this, we analysed the COSMO wind field both at the grid box in the Stuttgart basin as well as the wind field at the upwind southwestern boundary of the PALM-4U model domain (10 km each at the southern and western boundary). Figure 6a, b includes the COSMO wind speed profiles at 0300 and 0800 UTC. At 0300 UTC, the wind speed maximum is, in height and strength, close to the observed one. At 0800 UTC, the wind profile of COSMO is positioned between the observed and the simulated one. This means that the lateral forcing of PALM-4U by COSMO can only be partially held responsible for the analysed differences in the wind speed during night and morning hours.

4 Model evaluation of the vertical wind speed variance in the CBL

The synoptic conditions in the investigation area on 20 June 2018 were dominated by a high-pressure system stretching from France to Poland. This resulted in weak easterly winds of approximately 1–2 m s^{-1} in the CBL (Figure 7). Clear-sky conditions prevailed during daytime so that the global radiation reached up to 850 W m^{-2} around noon. Due to this, the near-surface layer became unstably stratified at around 0430 UTC, the daily maximum temperature reached approximately 35 °C. The near-surface layer became stably stratified again at around 1830 UTC. We restrict the model evaluation to the period from 0900 to 1800 UTC when pronounced convective activity was present in the CBL.

The diurnal evolution of z_i was determined from the backscatter signal of the ceilometer of SB station (Sec. 2.3.1). According to this, z_i in the morning grew constantly from about 450 m agl at 0900 UTC to about 1350 m agl at 1200 UTC (Figure 7a). The 1045 UTC radiosounding data from SB station shows that the z_i detection of the ceilometer agrees quite well with the well-mixed layer based on potential temperature and humidity data during this morning transition phase (difference of about 100 m, Figure 7a). In the afternoon, the z_i growth was weaker so that the CBL top reached about 1750 m agl at around 1600 UTC.

4.1 Vertical wind speed

Figure 8a, b presents the time-height cross sections of the vertical wind speed, w, at the two lidar sites TH and AFU (site locations see Figure 1c). Note that the maximum vertical range of the Windcube is 500 m agl only (Figure 8a). The horizontal distance between both observation sites is about 630 m. In the observations, the first considerable convection can be detected at both sites after about 0900 UTC. Until 1200 UTC, the convective updraughts at AFU reach the height of 1400 to 1500 m agl marking the entrainment zone (Figure 8b), which corresponds with the top of z_i due to the ceilometer data. Most of the deep thermals with updraught speeds up to 4 m s^{-1} extend from the surface to the entrainment zone. Periods with updraughts last about 30 to 45 min, interrupted by downdraughts of roughly the same order of duration (all well-known from textbooks like STULL (1988) or GARRATT (1992)). Although only 630 m apart, some pronounced differences in convective activity can be detected between the TH and AFU site. For example, at AFU, a period with mainly downdraughts can be found between about 1300 and 1500 UTC which is not visible at TH. This is also reflected in σ_w^2 discussed in Section 4.2.

Figure 8c, d shows the time-height cross sections of w from the PALM-4U simulation at TH and AFU. One striking feature is the much later onset of turbulence in the morning. There is no pronounced deeper convective activity simulated at TH before 1000 UTC and at AFU before 1100 UTC. This behaviour is investigated in more detail in Section 4.2. After that time, the simulations show similar patterns of convection as in the observations, also reaching approximately the same altitude as measured. However, the periods with strong updraughts between the two sites differ in time. The z_i grows from about 350 m agl at 0930 UTC to about 1200 m agl at 1200 UTC, i.e., the growth rate corresponds to the observed one (Figure 7).
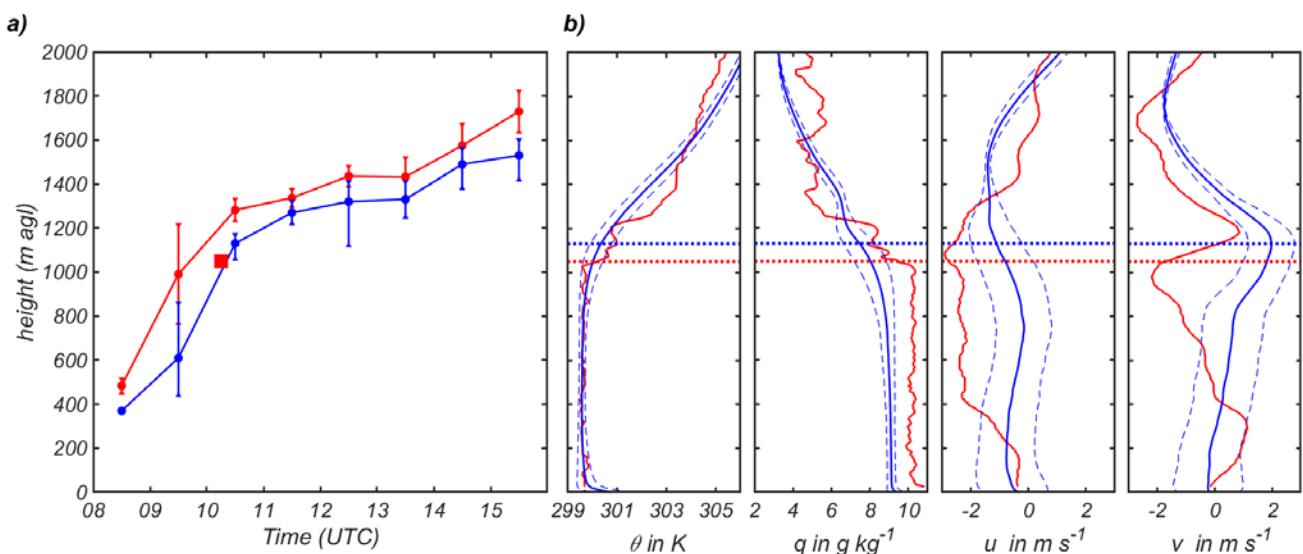
Figure 7: (a) Diurnal evolution of z_i based on the radiosonde at SB (red square), ceilometer at SB (red line, including uncertainty) (site locations see Figure 1c) and PALM-4U simulations for a 3 x 3 km^2 area in the Stuttgart basin (blue line, including uncertainty) on 20 June. (b) profiles of the potential temperature, Θ, specific humidity, q, u- and v-wind components of wind speed of the radiosounding at SB at 1045 UTC (solid red line) and simulation (mean value and uncertainty for the 3 x 3 km^2 area) at 1100 UTC (blue solid and dashed lines). The dotted lines indicate the corresponding z_i heights from observations (red) and simulation (blue).

Meteorol. Z. (Contrib. Atm. Sci.)
Early Access Article, 2024

Olga Kiseleva et al.: Evaluation of the Urban Climate Model PALM-4U

15
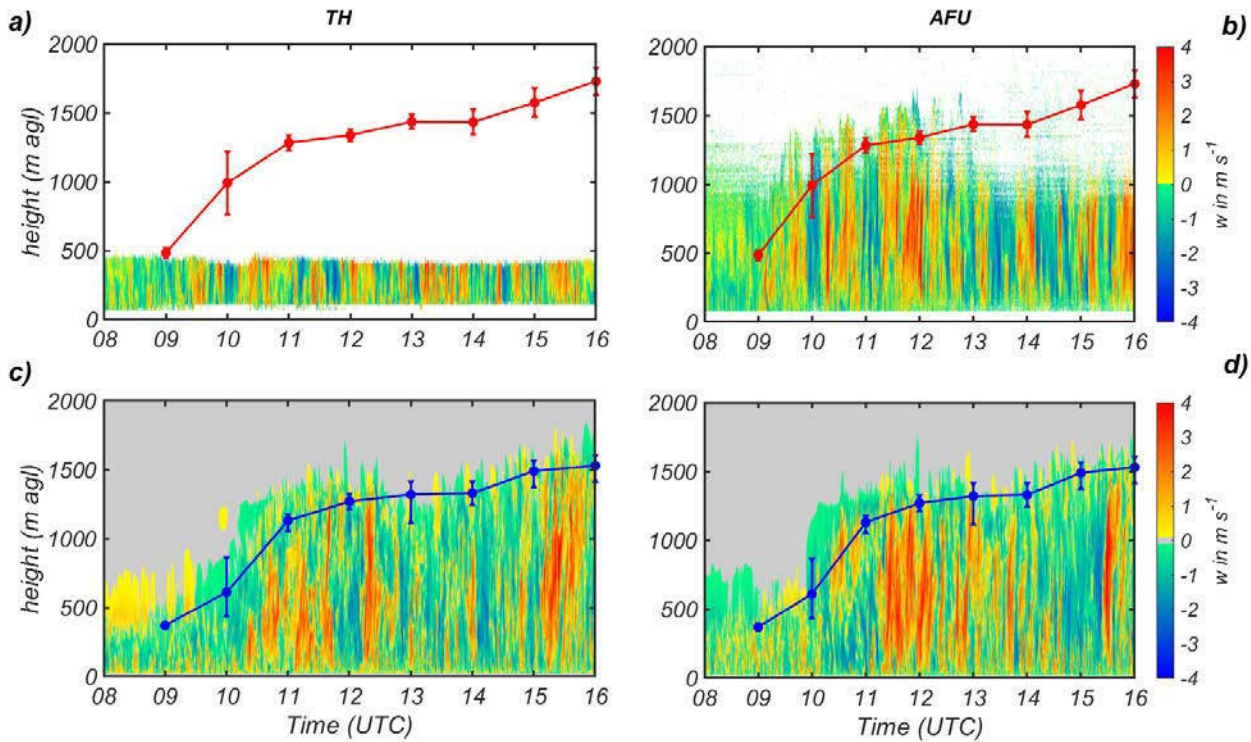
Figure 8: Time-height cross sections of vertical wind speed, w, measured at the two observational sites (a) TH and (b) AFU and (c,d) the corresponding values from the PALM-4U simulation on 20 June (site locations see Figure 1c). z_i (red line including uncertainty) in a) and b) is based on the ceilometer data from SB and z_i (blue line including uncertainty) in c) and d) is determined for the 3 x 3 km² area (see Figure 1c). In c) and d), the grey colour indicates vertical wind speed values between -0.1 and 0.1 m s⁻¹.

4.2 Vertical wind speed variance

In this section, the measured and simulated σ_w^2 values are compared. Additionally, the impact of the averaging period and the role of spatial variability are discussed. The motivation for this is that common integration intervals of $\mathcal{O}(1\,h)$ in boundary-layer studies may be critical in terms of representativity of σ_w^2 (e.g. MAURER et al., 2016). As our simulations provide high spatial resolution model output, they allow to investigate this issue in more detail. In the following, we discuss time series of σ_w^2 (Sec. 4.2.1) and vertical profiles of σ_w^2 (Sec. 4.2.2).

4.2.1 Times series of the vertical wind speed variance

Concerning the comparison of the diurnal cycle of σ_w^2 in the CBL, we used the continuous wind lidar measurements and simulation at the height of 350 m agl of TH and AFU. This height was selected as measured data are available at both sites. The σ_w^2 is calculated as 1-h moving averages (10 s shifted). Additionally, we determined spatial variances from the simulated vertical wind speed field of a 3 x 3 km²-sized area, which includes the TH and AFU sites (area see Figure 1c). These spatial variances are indicated as $\sigma_{w,3\times3}^2$.

Two main time intervals can be distinguished (Figure 9a). In the main growing phase of the CBL until 1100 UTC, the measured σ_w^2 values at TH and AFU reached up to more than 2 m²s⁻², while the simulated ones

varied between about 0.5 and 1.5 m²s⁻² only. The reason for these differences will be explained further below.

The second phase covers the period in which z_i is rather stationary (Figure 7), i.e., after 1100 UTC. At both measurement sites, temporal σ_w^2 variations in the order of 1 m²s⁻² occur. This holds for the measured and simulated 1-h moving averages of σ_w^2. Additionally, considerable spatial deviations of σ_w^2 between TH and AFU are visible (Figure 9a). For example, at about 1145 and 1315 UTC, the differences of measured σ_w^2 reach about 0.5 m²s⁻². The times with these differences coincide with those of greater differences in convection activities between TH and AFU (Figs. 8a,b and 9a). During some periods, the simulated σ_w^2 values at TH and AFU even reached differences of $\Delta\sigma_w^2(1100\,\text{UTC}) > 1.5$ m²s⁻² or $\Delta\sigma_w^2(1200\,\text{UTC}) \approx 0.7$ m²s⁻². More insight is provided by looking at the cumulative integral of the spectrum of $\sigma_w^2(t)$, where t is the oscillation period t = f⁻¹ and f is frequency (Figure 10). For the time intervals when considerable measured differences of σ_w^2 occur (e.g., 1115–1215 UTC and 1245–1345 UTC), $\sigma_w^2(t)$ of TH and AFU increase similarly at smaller oscillation periods (Figure 10b, c). Concerning 1115–1215 UTC, this is until ≈ 25 min, and concerning 1245–1345 UTC, this is until ≈ 10 min. Consequently, the main measured differences between σ_w^2 at TH and AFU are caused by turbulent structures with greater oscillation times. Concerning the simulations of σ_w^2 at TH and AFU during this time interval, the separation occurs for oscillation periods $\gtrsim 15$ min each (Figure 10b, c). To conclude:
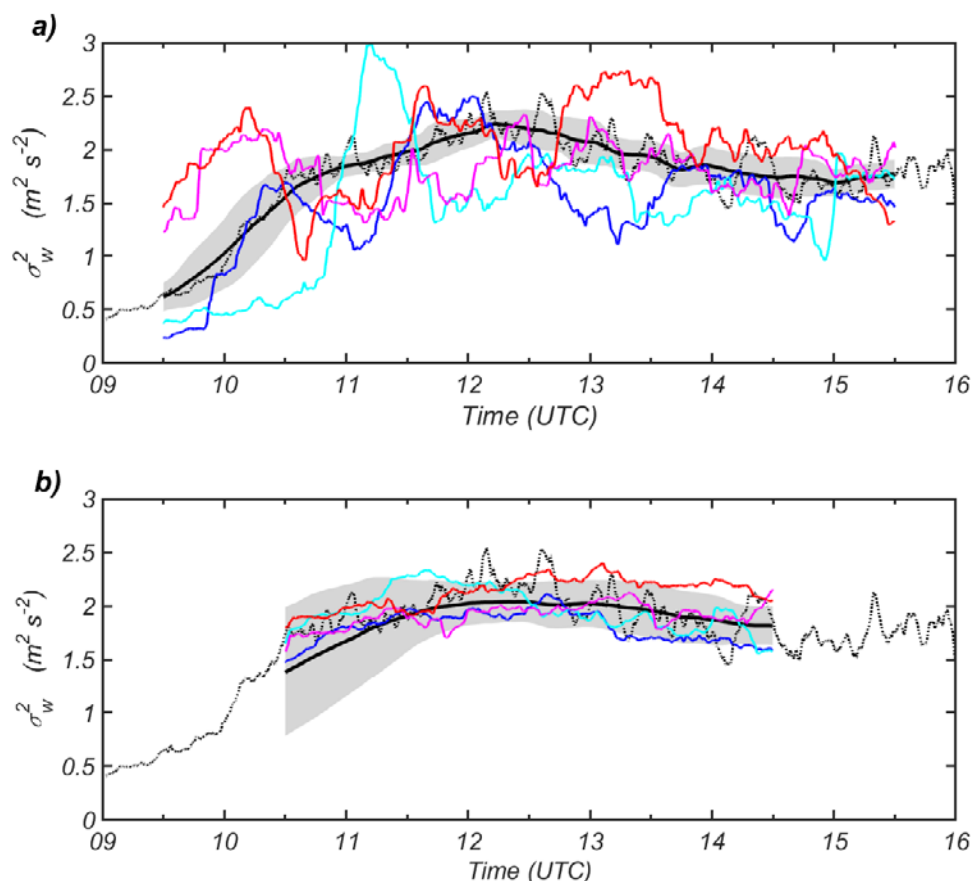
Figure 9: Time series of σ_w^2 at 350 m agl (a) based on 1-h moving averages and (b) on 3-h moving averages from observations at TH (red) and AFU (magenta) and simulations at TH (blue) and AFU (cyan) on 20 June (site locations see Figure 1c). The dotted black lines in a) and b) show $\sigma_{w,3\times3}^2$ and the solid black lines in a) show 1-h and in b) 3-h moving averages of $\sigma_{w,3\times3}^2$ including standard deviation (gray shading). The 3 x 3 km^2 area is indicated in Figure 1c.
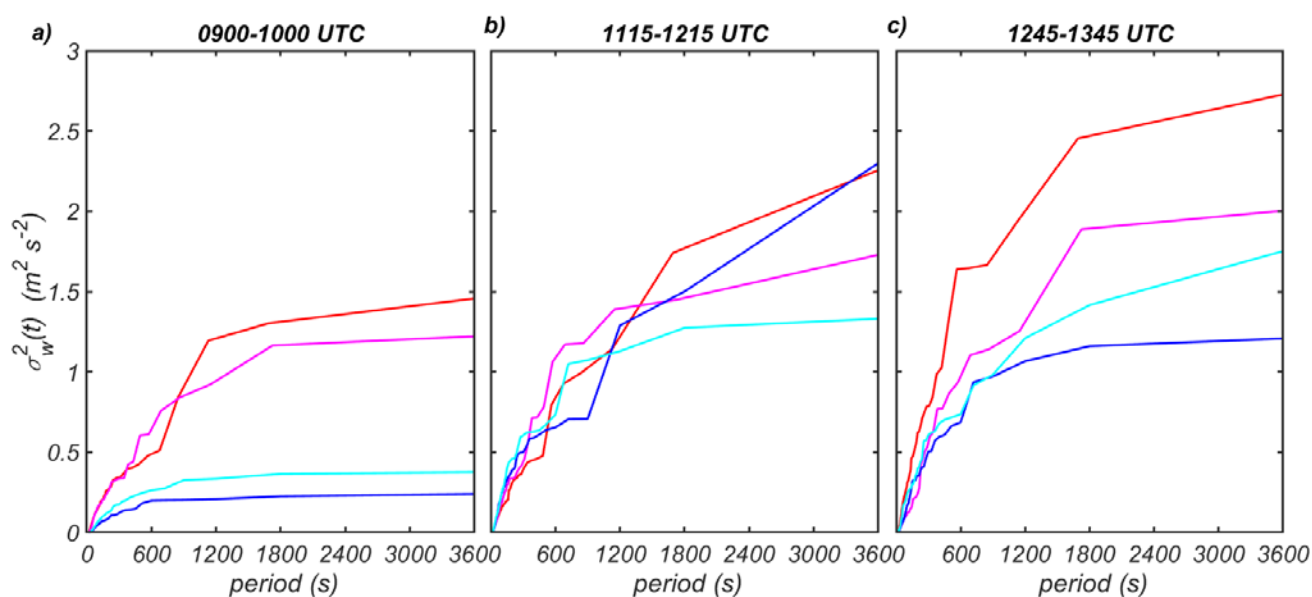
Figure 10: Cumulative integral of the spectrum of $\sigma_w^2(t)$ at 350 m agl as a function of the oscillation period, t=f^{-1} from observations at TH (red) and AFU (magenta) and simulations at TH (blue) and AFU (cyan) on 20 June (site locations see Figure 1c).
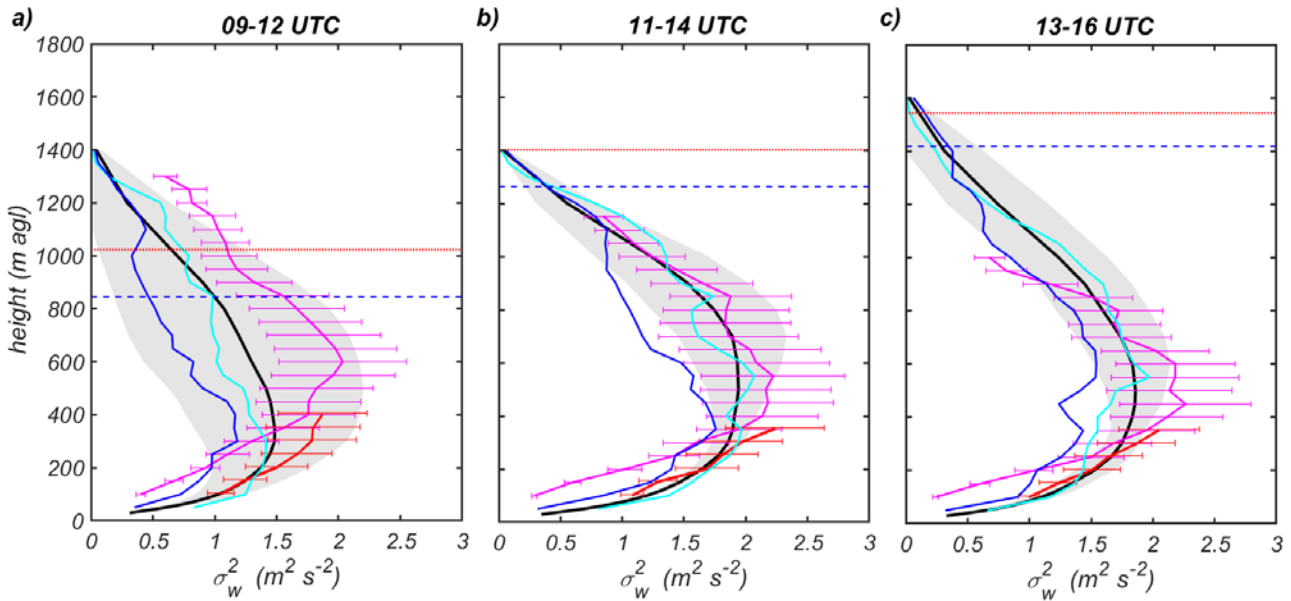
Figure 11: Vertical profiles of σ_w^2 from observations of TH (red) and AFU (magenta) including error bars and simulations of TH (blue) and AFU (cyan) (site locations see Figure 1c) for the time periods (a) 0900–1200 UTC, (b) 1100–1400 UTC, and (c) 1300–1600 UTC on 20 June. The black solid line indicates the 3-h means of $\sigma_{w,3\times3}^2$ including standard deviation based on the 15-min values (grey shaded). Horizontal lines show zi based on the observation (dotted red line) and simulation (dashed blue line).

using 1-h integration intervals, the relative differences of σ_w^2 between two adjacent measurement sites (distance of 630 m) as well as the relative differences between measured and simulated σ_w^2 values could even reach up to $\approx 50\%$. As σ_w^2 is dominated by turbulent structures at greater oscillation times, we suppose that the evaluation of PALM-4U based on 1-h integration times from measurements at single measurement sites – due to poor statistics – are not meaningful. In contrast to the diurnal cycles of σ_w^2 of the individual sites, $\sigma_{w,3\times3}^2$, shows a much smoother temporal behaviour (Figure 9a). Obviously, the vertical wind on the 3 x 3 km² area includes enough of the convective cells which determine the vertical wind speed variance. We compared the simulated σ_w^2 values of TH and AFU with $\sigma_{w,3\times3}^2$ to estimate the representativity of the measurements of these individual sites. This is done based on the NRMSE. Using a daily mean of $\sigma_w^2 = 1.8$ m²s⁻² for normalisation (Figure 9a, solid black line), the NRMSE $\approx 17\%$ for TH and $\approx 22\%$ for AFU. Hence, σ_w^2 values at individual sites and for 1-h intervals could be assumed to be associated with considerable uncertainties due to poor statistics. Thus, they seem to be only conditionally suitable for model evaluation. How many lidars would be useful under calm wind conditions providing statistically robust results (e.g. NRMSE < 10%) for model evaluation will be addressed in Section 4.3.

Since the number of measurement sites cannot be increased in hindsight, we increased the integration time to 3 hours. For them, the σ_w^2 values coincide much better (Figure 9b). This holds for the measurement and simulation results alike. For example, the relative deviations of measured σ_w^2 between TH and AFU at around 1145 and 1315 UTC decreased from $\approx 40\%$ for an integration time of 1 h to $\approx 10\%$ for an integration time

of 3 h (Figure 9a, b). Additionally, it can be concluded that the simulated 3-h moving average of $\sigma_{w,3\times3}^2$ fits with the measured σ_w^2. Relative deviations are < 15% (Figure 9b). Note that the high standard deviation of the simulated 3-h moving average of $\sigma_{w,3\times3}^2$ in the morning hours is due to the low σ_w^2 values before approximately 1100 UTC (Figure 9a).

4.2.2 Vertical profiles of the vertical wind speed variance

In consequence of the previous findings, we used 3-h integration times for the model evaluation of σ_w^2 for three selected time intervals (Figure 11). Shown are measured σ_w^2 profiles including error bars (according to LENSCHOW and KRISTENSEN, 1985; LENSCHOW et al., 1994) for TH and AFU and the corresponding simulation results as well as $\sigma_{w,3\times3}^2$ profiles including standard deviations. The differences between measured σ_w^2 at TH and AFU in the lowest about 300 m during all time intervals could be due the fact that turbulence at AFU – which is close to the slopes (Figure 1c) – is affected by slope winds and/or even by the lower density of buildings (Figure 1d). That means, larger symmetric eddies are disturbed more by the terrain (ZEEMAN et al., 2022). For the time interval from 0900 to 1200 UTC, the measured maximum of σ_w^2 at approximately 600 m agl is ≈ 2 m²s⁻² (available only for σ_w^2 at AFU) while the simulated maxima of σ_w^2 at TH and AFU as well as of $\sigma_{w,3\times3}^2$ are approximately at 300 m agl and are < 1.5 m²s⁻² (Figure 11a). Additionally, the standard deviation of $\sigma_{w,3\times3}^2$ is quite high (0.5 m²s⁻²). Note that in the simulation, pronounced convection before 1100 UTC is limited to levels below 500 m (Figs. 8c, d, and 9a). Consequently, the simulated profiles of TH and AFU above 400 m agl lie outside of the error bars estimated

for the measured profile (Figure 11a). We suppose that the main reason for the simulated slow growth of z_i in the morning to 400 m agl at 1000 UTC is caused by the approximately 500 m deep and 5 K strong NBL. The erosion of this NBL occurs later in the simulation than in the observation and the delayed erosion is responsible for the lower simulated variance of w compared to the measured variance of w at 350 m agl in the morning (Figure 9a).

Between 1100 and 1400 UTC, the simulated and observed z_i vary between approximately 1250 and 1400 m agl, respectively (Figure 11b). Between 1300 and 1600 UTC, z_i did not increase that much anymore (Figure 11c) being 1400 m agl in the simulation and approximately 1550 m agl in the observation. This means that for the two periods, the CBL conditions could be assumed to be nearly stationary. During the early-afternoon period, the measured and simulated σ_w^2 profiles at AFU reach a σ_w^2 maximum of approximately 2 m²s⁻² around 500 to 600 m agl, i.e., in the middle of the CBL (Figure 11b). For this time interval, the simulated σ_w^2 at AFU and $\sigma_{w,3\times3}^2$ lie – except for a few lower levels – within the error bars of the observation. The same findings also hold for the results of the time interval from 1300 to 1600 UTC (Figure 11c). Note that the $\sigma_{w,3\times3}^2$ profiles exhibit the smoothest profiles which again confirms the finding that for model evaluation, spatial information, e.g., achievable with an array of lidars, would be helpful to provide data with good statistics. Hence, using 3-h integration times, except for the non-stationary morning transition period, the vertical wind speed variances between simulations and observations agree considering the given uncertainty.

4.3   Discussion

We found that under high air pressure conditions, where wind speed is weak i.e., typically in the order of about 1 to 3 m s⁻¹, integration times of 1 h could be insufficient to provide turbulence parameters with good statistics (e.g., NRMSE $<\pm10\%$). On the other hand, assuming stationary conditions is usually not valid for periods longer than 1 h. Thus, extending the integration time is not a suitable option. Therefore, we investigate the other option to yield good statistics for σ_w^2, namely to increase the number of lidars in the field. The wavelength at the spectral peak, λ_m, usually represents the size of eddies with the most energy (KAIMAL and FINNIGAN, 1994). According to previous observational studies (e.g., KAIMAL et al., 1976; CAUGHEY and PALMER, 1979; ADLER et al., 2019), this wavelength relates to $\lambda_m \approx 1.5z_i$ at altitudes near the centre of the CBL. With z_i being of the order of $\mathcal{O}(1\,\text{km})$ (Figure 7), this yields $\lambda_m \approx 1.5\,\text{km}$. To resolve eddies $\geq \lambda_m$, in analogy to the Nyquist frequency, the horizontal distance, Δ, between lidars should be approximately 750 m. We used a 10-s model output with 10 m grid spacing at 350 m agl of the 3 x 3 km² area as reference of "true" variance. This corresponds to an array with 90000 virtual lidars. From that value, we then successively reduced the number of lidars, N, respectively increased Δ between them from N=3480/Δ=50 m, N=840/Δ=100 m via N=36/Δ=400 m, N=25/Δ=500 m, N=9/Δ=700 m down to N=4/Δ=1000 m. By this, we estimated how many lidars would be necessary to represent the "true" σ_w^2 value. For an array with 840 lidars, their mean σ_w^2 shows a quite low NRMSE < 0.5% (RMSE < 0.007 m²s⁻²) (Figure 12). For lidar numbers of 36 or 25, their mean σ_w^2 values result in NRMSE of < 6% (RMSE < 0.08 m²s⁻². Using nine lidars results in NRMSE ≈ 4% (RMSE ≈ 0.04 m²s⁻²) in the morning and NRMSE ≈ 8% (RMSE ≈ 0.13 m²s⁻²) during noon and afternoon and finally, using four lidars results in NRMSE ≈ 9% (RMSE ≈ 0.09 m²s⁻²) in the morning and NRMSE ≈ 12% (RMSE ≈ 0.19 m²s⁻²) during noon and afternoon. This means that to assure good quality data, approximately nine lidars should be installed on days with calm wind
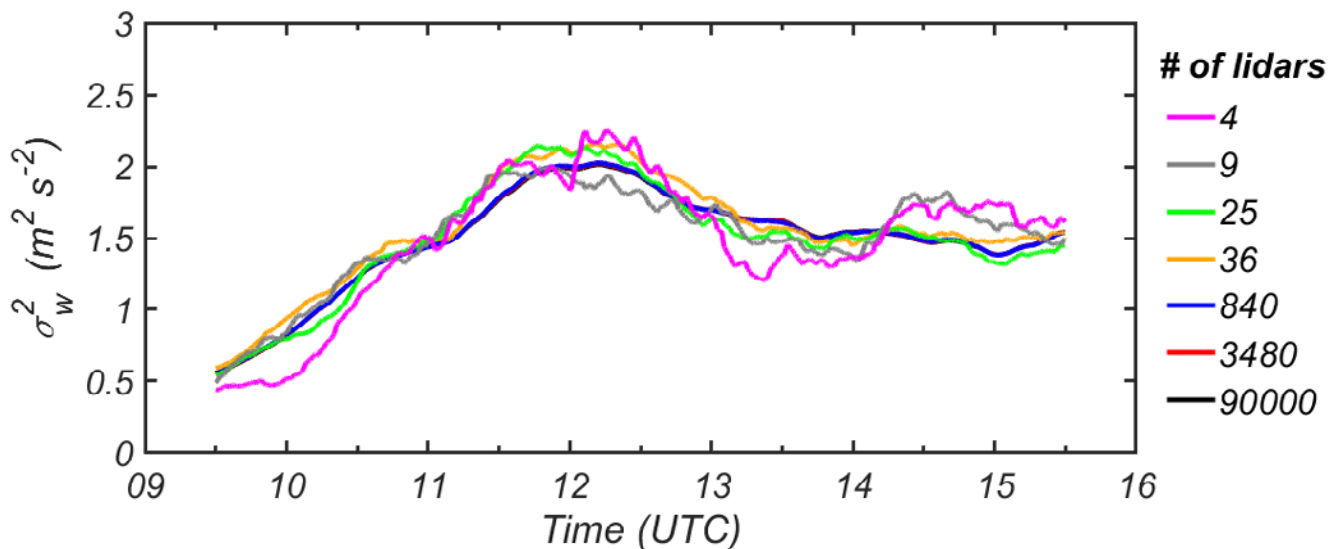
Figure 12: Simulated time series of σ_w^2 at 350 m agl based on 1-h moving averages using virtual lidar arrays on 20 June (area see Figure 1c) with different numbers of lidars and different lidar distances (see text) between them.

Meteorol. Z. (Contrib. Atm. Sci.)
Early Access Article, 2024

Olga Kiseleva et al.: Evaluation of the Urban Climate Model PALM-4U

19

conditions. This seems to be a lot, but this number of lidars was already deployed in recent experiments. For example, about 20 wind lidars were deployed during the Perdigão experiment (Vasiljević et al., 2015; Mann et al., 2018), and nine wind lidars were available for the FESSTVaL experiment (Lundgren et al., 2022).

Arrays with 5 x 5 lidar pairs distributed over an area of 3 x 3 km² with distances of 750 m between them turned out to be suitable for σ_w^2 measurements with requested accuracy for entirely calm wind conditions. In addition, 25 lidars is still an affordable number. Therefore, we use this approach to estimate the impact of wind speed on the uncertainty of σ_w^2. It is assumed that the uncertainty of σ_w^2 remains the same if the number of λ_m-sized cells scanned by wind lidars during a 1-h sampling period remains the same. For a wind speed of U=1 m s⁻¹, in time T=1 h, the λ_m-sized cells are transported over a distance of $L_x \approx 3.5$ km, i.e, over our virtual lidar array. Increasing the wind speed to 2 m s⁻¹, the cells are transported over $L_x \approx 7$ km, so that the array in y-direction could be halved, which corresponds to a lidar number of 12 to 13. In the case of a wind speed of 3 m s⁻¹, the $L_x \approx 11$ km and the number of lidars in y-direction could be divided by 3 so that the lidar array could consist of 7 to 8 lidars. Our results indicate that evaluations of eddy-resolving CBL simulations with σ_w^2 measurements from a small number of wind lidars should target weather situations with moderate regional winds rather than entirely calm wind conditions.

5 Summary and conclusion

The objective of this study was to evaluate the city climate model PALM-4U concerning its representation of dynamical and turbulent conditions in the ABL over complex terrain. For this purpose, we used data from the [UC]2 summer campaigns conducted in Stuttgart in 2017 and 2018 (Kiseleva et al., 2021; Samad et al., 2023). We selected a two-day episode in 2017 to evaluate the flow field under stable and unstable conditions and a day in 2018 to evaluate σ_w^2 in the boundary layer under convective conditions.

The flow field in 2017 was compiled from in-situ and remote sensing vertical profiling as well as the virtual-tower techniques using Doppler lidars to measure wind profiles at several sites. In 2018, two Doppler lidars were operated in vertical stare mode at the TH and AFU sites in the Stuttgart basin to measure vertical wind speed to provide σ_w^2 profiles.

PALM-4U was off-line nested in the COSMO model. For the 2017 episode, the model domain was 48 x 48 x 4 km³ in x-, y-, and z-direction, respectively, the grid spacing was 40 m and model output was every 10 min. For the 2018 episode, the model domain was 12 x 12 x 2.5 km³ with grid spacings of 10 m. Standard model output for the whole model domain was every hour. Additionally, the vertical wind speed was stored every 10 s for a box of 100 m diameter around the lidar sites TH and AFU.

The main findings of this study are:

- PALM-4U properly simulated the depth and strength of the nocturnal boundary layer and the evolution of the daytime boundary-layer depth.
- Concerning the wind field evaluation, we focused on the levels at about 100 and 700 m agl. The first level provides the daytime conditions in the surface layer of the CBL and nighttime conditions of the NBL and the second level provides the daytime conditions in the mixed layer of the CBL and the nighttime conditions in the RL. Overall, PALM-4U provided a good agreement with the observed diurnal cycle of the wind in the investigation area. Good agreement means: the NRMSE values of wind speed at 100 m agl for the first 21 hours and the whole 36 hours are about 0.5 and 0.9, respectively. For wind direction RMSE values are about 35°. For the 700 m agl level, the NRMSE value of wind speed is 0.2–0.3 and RMSE of wind direction is about 15°. The considerable differences between observed and simulated wind speed in the Stuttgart basin at 100 m agl during the last 15 hours (night from 14 to 15 August and morning of 15 August) are associated with the underestimated height and overestimated strength of the simulated nocturnal LLJ. This is reflected in lower bulk Richardson numbers at lower levels in the simulation allowing enhanced downward mixing of momentum and the associated higher wind speed. Concerning the uncertainty of PALM-4U nighttime simulations, ensemble simulations could be an appropriate approach to quantify the uncertainty in more detail.
- Concerning σ_w^2 based on 1-h integration times, the measured moving averages of σ_w^2 at TH and AFU showed variations of up to 50% in time as well as between both sites, although both sites were only 630 m apart. The different locations relative to the basin centre accompanied by different underlying building density could be one reason for the deviations. A similarly high difference was found for the comparison of observed and simulated σ_w^2 values. The cumulative spectrum of σ_w^2 revealed that the difference in the variance between the two sites was dominated by turbulence structures of 10 to 25 min oscillation periods and explained the poor statistics associated with 1-h intervals. Thus, they seem to be of insufficient robustness for model evaluation.
- Using 3-h integration times for the σ_w^2 calculation, the simulated profiles of σ_w^2 lie within the error bars of the observed σ_w^2 profiles.

In summary it can be concluded that PALM-4U simulates wind fields, turbulence and diurnal boundary layer development with sufficient accuracy for the intended use as a high-resolution city climate model.

Additional to the model evaluation, the model simulations can be used to estimate the number of wind lidars needed to guarantee an uncertainty of e.g. NRMSE < 10% for σ_w^2. Our following considerations assume almost stationarity conditions (i.e., allowing only 1-h integration

intervals) and calm winds. Reducing the initial number of virtual lidars (90000) and in parallel increasing the initial 10-m distance between them, it turned out that arrays with 9 to 25 lidars provide σ_w^2 with NRMSE of < 10%. Note that 9 to 25 lidars are a realistic number of available lidars as already deployed in previous experiments (e.g., 20 wind lidars in the Perdigão experiment (Vasiljević et al., 2017; Mann et al., 2018) and 8 wind lidars in the FESSTVaL experiment (Lundgren et al., 2022)). When the calm wind (1 m s^{-1}) is doubled or tripled, theoretical considerations suggest that the number of lidars could be reduced to about 12 and 8, respectively, to achieve the same degree of uncertainty. Hence, for experiments designed to receive variance or covariance data in the CBL for model evaluation, it is recommended – in case that only a limited number of lidars are available – to assure that synoptic conditions with rather moderate than calm winds prevail.

Acknowledgments

References

Adler, B., N. Kalthoff, O. Kiseleva, 2020: Detection of structures in the horizontal wind field over complex terrain using coplanar doppler lidar scans. – Meteorol. Z. **29**, 467–481, DOI: 10.1127/metz/2020/1031.

Adler, B., O. Kiseleva, N. Kalthoff, A. Wieser, 2019: Comparison of convective boundary layer characteristics from aircraft and wind lidar observations. – Atmos. Oceanic Technology **36**, 1381–1399, DOI: 10.1175/JTECH-D-18-0118.1.

Ansmann, A., J. Fruntke, R. Engelmann, 2010: Updraft and downdraft characterization with Doppler lidar: cloud-free versus cumuli-topped mixed layer. – Atmos. Chem. Phys. **10**, 7845–7858, DOI: 10.5194/acp-10-7845-2010.

Angevine, W. M., R. J. Doviak, Z. Sorbjan, 1994: Remote sensing of vertical velocity variance and surface heat flux in a convective boundary layer. – J. Appl. Meteor. **33**, 977–983. DOI: 10.1175/1520-0450(1994)0332.0.CO;2.

Babić, K., B. Adler, N. Kalthoff, H. Andersen, C. Dione, F. Lohou, M. Lothon, X. Pedruzo-Bagazgoitia, 2019: The observed diurnal cycle of low-level stratus clouds over southern West Africa: a case study. – Atmos. Chem. Phys. **19**, 1281–1299. DOI: 10.5194/acp-19-1281-2019.

Banta, R.M., Y.L. Pichugina, R.K. Newsom, 2003: Relationship between low-level jet properties and turbulence kinetic energy in the nocturnal stable boundary layer. – J. Atmos. Sci. **60**, 2549–2555. DOI: 10.1175/1520-0469(2003)0602.0.CO;2.

Baumbach, G., U. Vogt, S. Hansen, 1999: Messungen der Kaltluftströme und Luftverunreinigungs- Vertikalprofile im Plangebiet "Stuttgart 21". Heft 15, Schriftenreihe Untersuchungen zur Umwelt "Stuttgart 21". Hrsg.: Landeshaupstadt Stuttgart, Amt für Umweltschutz.

Baumbach, G., U. Vogt, 2003: Influence of inversion layers on the distribution of air pollutants in urban areas. – Water, Air, & Soil Pollution: Focus **3**, 67–78, DOI: 10.1023/A:1026098305581.

Caughey, S. J., S. G. Palmer, 1979: Some aspects of turbulence structure through the depth of the convective boundary layer. – Quart. J. Roy. Meteor. Soc. **105**, 811–827, DOI: 10.1002/qj.49710544606.

Corsmeier, U., N. Kalthoff, O. Kolle, M. Kotzian, F. Fiedler, 1997: Ozone concentration jump in the stable nocturnal boundary layer during a LLJ-event. – Atmos. Environ. **31**, 1977–1989. DOI: 10.1016/S1352-2310(96)00358-5.

Damian, T., A. Wieser, K. Träumner, U. Corsmeier, C. Kottmeier, 2014: Nocturnal low-level jet evolution in a broad valley observed by dual Doppler lidar. – Meteorol. Z. **23**, 305–313, DOI: 10.1127/0941-2948/2014/0543.

Eng, K., R. L. Coulter, W Brutsaert, 2003: Vertical velocity variance in the mixed layer from radar wind profilers. – J. Hydrol. Eng. **8**, 301–307, DOI: 10.1061/(ASCE)1084-0699(2003)8:6(301).

Garratt, J.R., 1992: The atmospheric boundary layer. Cambridge University Press, ISBN-10 0521380529.

Geletič, J., M. Lehnert, P. Krč, J. Resler, E.S. Krayenhoff, 2021: High-resolution modelling of thermal exposure during a hot spell: a case study using PALM-4U in Prague, Czech Republic. – Atmosphere **12**, 175, DOI: 10.3390/atmos12020175.

Giovannini, L., L. Laiti, S. Serafin, D. Zardi, 2017: The thermally driven diurnal wind system of the Adige Valley in the Italian Alps. – Quart. J. Roy. Meteor. Soc. **143**, 2389–2402, DOI: 10.1002/qj.3092.

Halbig, G., B. Steuri, B. Büter, I. Heese, J. Schultze, M. Stecking, S. Stratbücker, L. Willen, M. Winkler, 2019: User requirements and case studies to evaluate the practicability and usability of the urban climate model PALM-4U. – Meteorol. Z. **28**, 139–146. DOI: 10.1127/metz/2019/0914.

Heldens, W., C. Burmeister, F. Kanani-Sühring, B. Maronga, D. Pavlik, M. Sühring, J. Zeidler, T. Esch, 2020: Geospatial input data for the PALM model system 6.0: model requirements, data sources and processing. – Geosci. Model Dev. **13**, 5833–5873, DOI: 10.5194/gmd-13-5833-2020.

Hogan, R. J., A. L. Grant, A. L. Illingworth, G.N. Pearson, E.J. O'Connor, 2009: Vertical velocity variance and skewness in clear and cloud-topped boundary layers as revealed by Doppler lidar. – Quart. J. Roy. Meteor. Soc. **135**, 635–643, DOI: 10.1002/qj.413.

Kadasch, E., M. Sühring, T. Gronemeier, S. Raasch, 2021: Mesoscale nesting interface of the PALM model system 6.0, Geosci. – Model Dev. **14**, 5435–5465, DOI: 10.5194/gmd-14-5435-2021.

Kaimal, J. C., J.C. Wyngaard, D.A. Haugen, O.R. Coté, Y. Izumi, S.J. Caughey, C.J. Readings, 1976: Turbulence

Meteorol. Z. (Contrib. Atm. Sci.)
Early Access Article, 2024

Olga Kiseleva et al.: Evaluation of the Urban Climate Model PALM-4U

21

structure in the convective boundary layer. – J. Atmos. Sci. **33**, 2152–2169, DOI: 10.1175/1520-0469(1976)0332.0.CO;2.

KAIMAL, J. C., J. J. FINNIGAN, 1994: Atmospheric boundary layer flows: Their structure and measurements. Oxford University Press, ISBN 0-19-506239-6. DOI: 10.1093/oso/9780195062397.001.0001.

KIM, Y., I.P. CASTRO, Z.-T. XIE, 2013: Divergence-free turbulence inflow conditions for large-eddy simulations with incompressible flow solvers. – Comput. Fluids **84**, 56–68, DOI: 10.1016/j.compfluid.2013.06.001.

KISELEVA, O., B. ADLER, N. KALTHOFF, M. KOHLER, A. WIESER, N. WITTKAMP, 2019: Data set of meteorological observations (wind, temperature, humidity) collected from a microwave radiometer and lidar measurements during four intensive observations periods in 2017 and 2018 in Stuttgart, Germany, under the BMBF Programme 'Urban Climate Under Change' [UC]2). DOI (KIT): DOI: 10.5445/IR/1000093534., KITopen-ID: 1000093534.

KISELEVA, O., N. KALTHOFF, B. ADLER, M. KOSSMANN, A. WIESER, R. RINKE, 2021: Nocturnal atmospheric conditions and their impact on air pollutant concentrations in the city of Stuttgart. – Meteorol. Appl. **28**, Article no: e2037. DOI: 10.1002/met.2037.

KOTTHAUS, S., J. A. BRAVO-ARANDA, M. COLLAUD COEN, J.L. GUERRERO-RASCADO, M.J. COSTA, D. CIMINI, E.J. O'CONNOR, M. HERVO, L. ALADOS-ARBOLEDAS, M. JIMÉNEZ-PORTAZ, L. MONA, D. RUFFIEUX, A. ILLINGWORTH, M. HAEFFELIN, 2023: Atmospheric boundary layer height from ground-based remote sensing: a review of capabilities and limitations. – Atmos. Meas. Tech. **16**, 433–479. DOI: 10.5194/amt-16-433-2023.

LANDSBERG, H. E., 1981: The urban climate. Academic Press. New York. ISBN 0-12-435960-4.

LENSCHOW, D. H., L. KRISTENSEN, 1985: Uncorrelated noise in turbulence measurements. – J. Atmos. Oceanic Technol. **2**, 68–81. DOI: 10.1175/1520-0426(1985)0022.0.CO;2.

LENSCHOW, D. H., J.C. WYNGAARD, W.T. PENNELL, 1980: Mean-field and second-moment budgets in a baroclinic, convective boundary layer. – J. Atmos. Sci. **37**, 1313–1326, DOI: 10.1175/1520-0469(1980)0372.0.CO;2.

LENSCHOW, D. H., J. MANN, L. KRISTENSEN, 1994: How long is long enough when measuring fluxes and other turbulence statistics? – J. Atmos. Oceanic Technol. **11**, 661–673. DIO: DOI: 10.1175/1520-0426(1994)0112.0.CO;2.

LENSCHOW, D.H., V. WULFMEYER, C. SENFF, 2000: Measuring second- through fourth-order moments in noisy data. – J. Atmos. Oceanic Technol. **17**, 1330–1347, DOI: 10.1175/1520-0426(2000)0172.0.CO;2.

LENSCHOW, D. H., M. LOTHON, S. D. MAYOR, P. P. SULLIVAN, G. CANUT, 2012: A comparison of higher-order vertical velocity moments in the convective boundary layer from lidar with in situ measurements and large-eddy simulation. – Boundary-Layer Meteorol. **143**, 107–123, DOI: 10.1007/s10546-011-9615-3.

LUNDGREN, K., C. HOHENEGGER, F. AMENT, F. BEYRICH, U. LÖHNERT, M. GÖBER, H. RUST, M. SAKRADZIJA, I. BASTAK-DURAN, M., MASBOU, A. JAHNKE-BORNEMANN, 2022: FESSTVaL: Field Experiment on sub-mesoscale spatio-temporal variability in Lindenberg – the campaign, first results and data availability, EGU General Assembly 2022, Vienna, Austria, 23–27 May 2022, EGU22-8889, DOI: 10.5194/egusphere-egu22-8889.

MAHRT, L., 1998: Flux sampling errors for aircraft and towers. – J. Atmos. Oceanic Technol. **15**, 416–429, DOI: 10.1175/1520-0426(1998)0152.0.CO;2.

MANN, J., R. MENKE, N. VASILJEVIĆ, J. BERG, N. TROLDBORG, 2018: Challenges in using scanning lidars to estimate wind resources in complex terrain. – J. Phys.: Conf. Ser. 1037 072017, DOI: 10.1088/1742-6596/1037/7/072017.

MARONGA, B., G. GROSS, S. RAASCH, S. BANZHAF, R. FORKEL, W. HELDENS, F. KANANI-SÜHRING, A. MATZARAKIS, M. MAUDER, D. PAVLIK, J. PFAFFEROTT, S. SCHUBERT, G. SECKMEYER, H. SIEKER, K. WINDERLICH, 2019: Development of a new urban climate model based on the model PALM – Project overview, planned work, and first achievements. – Meteorol. Z. **28**, 105–119. DOI: 10.1127/metz/2019/0909.

MARONGA, B., S. BANZHAF, C. BURMEISTER, T. ESCH, R. FORKEL, D. FRÖHLICH, V. FUKA, K.F. GEHRKE, J. GELETIČ, S. GIERSCH, T. GRONEMEIER, G. GROSS, W. HELDENS, A. HELLSTEN, F. HOFFMANN, A. INAGAKI, E. KADASCH, F. KANANI-SÜHRING, K. KETELSEN, B. ALI KHAN, C. KNIGGE, H. KNOOP, P. KRČ, M. KURPPA, H. MAAMARI, A. MATZARAKIS, M. MAUDER, M. PALLASCH, D. PAVLIK, J. PFAFFEROTT, J. RESLER, S. RISSMANN, E. RUSSO, M. SALIM, M. SCHREMPF, J. SCHWENKEL, G. SECKMEYER, S. SCHUBERT, M. SÜHRING, R. VON TILS, L. VOLLMER, S. WARD, B. WITHA, H. WURPS, J. ZEIDLER, S. RAASCH, 2020: Overview of the PALM model system 6.0. – Geosci. Model Dev. **13**, 1335–1372. DOI: 10.5194/gmd-13-1335-2020.

MARTUCCI, G., C. MILROY, C.D. O'DOWD, 2010: Detection of cloud-base height using Jenoptik CHM15K and Vaisala CL31 ceilometers. – J. Atmos. Oceanic Technol. **27**, 305–318, DOI: 10.1175/2009JTECHA1326.1.

MAURER, V., N. KALTHOFF, A. WIESER, M. KOHLER, M. MAUDER, L. GANTNER, 2016: Observed spatiotemporal variability of boundary-layer turbulence over flat, heterogeneous terrain. – Atmos. Chem. Phys. **16**, 1377–1400, DOI: 10.5194/acp-16-1377-2016.

MAYER, H., 1999: Air pollution in cities. – Atmos. Env. **33**, 4029–4037, DOI: 10.1016/S1352-2310(99)00144-2.

MILROY, C., G. MARTUCCI, S. LOLLI, S. LOAEC, L. SAUVAGE, I. XUEREF-REMY, J.V. LARIC, P. CIAIS, D.G. FEIST, G. BIAVATI, C.D. O'DOWD, 2012: Assessment of pseudo-operational ground-based light detection and ranging sensors to determine the boundary-layer structure in the coastal atmosphere. – Adv. Meteorol. **8**, 929080, DOI: 10.1155/2012/929080.

OKE, T.R., G. MILLS, C. CHRISTEN, J.A. VOOGT, 2017: Urban Climates. Cambridge University Press, Cambridge. ISBN 978-1-107-42953-6. DOI: 10.1017/9781139016476.

PANOFSKY, H.A., C. MAZZOLA, 1971: Variances and spectra of vertical velocity just above the surface layer. – Boundary-Layer Meteorol. **2**, 30–37, DOI: 10.1007/BF00718086.

RENDÓN, A.M., J.F. SALAZAR, C.A. PALACIO, V. WIRTH., B. BRÖTZ, 2014: Effects of urbanization on the temperature inversion breakup in a mountain valley with implications for air quality. – J. Appl. Meteorol. Climatol. **53**, 840–858, DOI: 10.1175/JAMC-D-13-0165.1.

REUTER, U., R. KAPP, 2021: Urban climate in urban planning: The experiences from Stuttgart, in Chapter 12: Urban Climate Science for Planning Healthy Cities, Editors C. Ren and G. McGregor, Springer Nature Publishing Cham, 259–284, DOI: 10.1007/978-3-030-87598-5_12.

RITTER, C., C. MÜNKEL, 2021: Backscatter Lidar for Aerosol and Cloud Profiling. – Springer Handbook of Atmospheric Measurements. Springer Cham, 685–719. DOI: 10.1007/978-3-030-52171-4_24.

RÖHNER, L., K. TRÄUMNER, 2013: Aspects of convective boundary-layer turbulence measured by dual-Doppler lidar system. – J. Atmos. Ocean. Technol. **30**, 2132–2142, DOI: 10.1175/JTECH-D-12-00193.1.

SAMAD, A., O. KISELEVA, C. HOLST, R. WEGENER, M. KOSSMANN, G. MEUSEL, A. FIEHN, T- ERBERTSEDER, R. BECKER, A. ROIGER, P. STANISLAWSKY, D. KLEMP, S. EMEIS, N. KALTHOFF, U. VOGT,

2023: Meteorological and air quality measurements in a city region with complex terrain: influence of meteorological phenomena on urban climate. – Meteorol. Z. **32**, 293 – 315, DOI: 10.1127/metz/2023/1124.

Schättler, U., G. Doms, C. Schraff, 2014: A Description of the Non-hydrostatic Regional COSMO-Model Part VII : User's Guide, Tech. rep., Deutscher Wetterdienst, P.O. Box 100465, 63004 Offenbach, Germany, available at: http://www.cosmo-model.org (last access: 31 August 2022).

Scherer, D., F. Antretter, S. Bender, J. Cortekar, S. Emeis, U. Fehrenbach, G. Gross, G. Halbig, J. Hasse, B. Maronga, S. Raasch, K. Scherber, 2019a: Urban Climate Under Change [UC]2 – A national research programme for developing a building-resolving atmospheric model for entire city regions. – Meteorol. Z. **28**, 95–104, DOI: 10.1127/metz/2019/0913.

Scherer, D., F. Ament, S. Emeis, U. Fehrenbach, B. Leitl, K. Scherber, C. Schneider, U. Vogt, 2019b: Three-dimensional observation of atmospheric processes in cities. – Meteorol. Z. **28**, 121–138, DOI: 10.1127/metz/2019/0911.

Sorbjan, Z., 1986: On similarity in the atmospheric boundary layer. – Boundary-Layer Meteorol. **34**, 377–397, DOI: 10.1007/BF00120989.

Steinfeld, G., M. Letzel, S. Raasch, M. Kanda, A. Inagaki, 2007: Spatial representativeness of single tower measurements and the imbalance problem with eddy-covariance fluxes: results of a large-eddy simulation study. – Boundary-Layer Meteorol. **123**, 77–98, DOI: 10.1007/s10546-006-9133-x.

Steuri, B., S. Bender, J. Cortekar, 2020: Successful user-science interaction to co-develop the new urban climate model PALM-4U. – Urban Climate **32**, 100630. DOI: 10.1016/j.uclim.2020.100630.

Steyn, D.G., S.F.J. de Wekker, M. Kossmann, A. Martilli, 2013: Boundary Layers and Air Quality in Mountainous Terrain, in Chapter 5: Mountain Weather Research and Forecasting – Recent Progress and Current Challenges, Editors F. K. Chow, S. F. J. de Wekker, B. Snyder, Springer Berlin, 261–290, DOI: 10.1007/978-94-007-4098-3_5.

Stull, R.B., 1988: An introduction to boundary layer meteorology. Springer Science & Business Media, ISBN-10. 9027727686. DOI: 10.1007/978-94-009-3027-8.

van Stratum, J.H. Bart., B. Stevens, 2015: The influence of misrepresenting the nocturnal boundary layer on idealized daytime convection in large-eddy simulation, – J. Adv. Model. Earth Syst. **7**, 423–436, DOI: 10.1002/2014MS000370.

Vasiljević, N., J. M. L. M. Palma, N. Angelou, J. C. Matos, R. Menke, G. Lea, J. Mann, M. Courtney, L. F. Ribeiro, V. M. M. G. C. Gomes, 2017: Perdigão 2015: Methodology for atmospheric multi-Doppler lidar experiments. – Atmos. Meas. Tech. **10**, 3463–3483, DOI: 10.5194/amt-10-3463-2017.

Wanner, H., J.A. Hertig, 1984: Studies of urban climates and air pollution in Switzerland. – J. Climate Appl. Meteor. **23**, 1614–1625, DOI: 10.1175/1520-0450(1984)0232.0.CO;2.

Winkler, M., B. Steuri, S. Stalder, F. Antretter, 2020: Evaluating the practicability of the new urban climate model PALM-4U using a living-lab approach. In: E3S Web of Conferences 172, 11010, EDP Sciences, DOI: 10.1051/e3sconf/202017211010.

Wittkamp, N., B. Adler, N. Kalthoff, O. Kiseleva, 2021: Mesoscale wind patterns over the complex urban terrain around Stuttgart investigated with dual-Doppler Lidar profiles. – Meteorol. Z. **30**, 185–200, DOI: 10.1127/metz/2020/1029.

Wyngaard, J. C., O.R. Coté, Y. Izumi, 1971: Local free convection, similarity, and the budgets of shear stress and heat flux. – J. Atmos. Sci. **28**, 1171–1182, DOI: 10.1175/1520-0469(1971)0282.0.CO;2.

Xie, Z., I. Castro, 2008: Efficient generation of inflow conditions for large-eddy simulation of street-scale flows. – Flow Turbul. Combust. **81**, 449–470, DOI: 10.1007/s10494-008-9151-5.

Young, G. S., 1988: Turbulence structure of the convective boundary layer. Part I. Variability of normalized turbulence statistics. – J. Atmos. Sci. **45**, 719–726, DOI: 10.1175/1520-0469(1988)0452.0.CO;2.

Zeeman, M., C.C. Holst, M. Kossmann, D. Leukauf, C. Münkel, A. Philipp, R. Rinke, S. Emeis, 2022: Urban boundary-layer structure in complex terrain: An empirical 3D case study for Stuttgart, Germany. – Front. Earth Sci. **10**, 840112, DOI: 10.3389/feart.2022.840112.